Investigation of reactive perovskite materials for solar fuel production via two-step redox cycles: thermochemical activity, thermodynamic properties and reduction kinetics

Anita Haeussler, Anne Julbe, Stéphane Abanades

To cite this version:

Anita Haeussler, Anne Julbe, Stéphane Abanades. Investigation of reactive perovskite materials for solar fuel production via two-step redox cycles: thermochemical activity, thermodynamic properties and reduction kinetics. Materials Chemistry and Physics, 2022, 276, pp.125358. 10.1016/j.matchemphys.2021.125358 . hal-03530154

HAL Id: hal-03530154
https://hal.science/hal-03530154v1

Submitted on 17 Jan 2022

Investigation of reactive perovskite materials for solar fuel production via two-step redox cycles: thermochemical activity, thermodynamic properties and reduction kinetics

Anita HAEUSSLER [a], Anne JULBE [b], Stéphane ABANADES [a] *

[a] Processes, Materials and Solar Energy Laboratory, CNRS-PROMES, 7 Rue du Four Solaire, 66120 Font-Romeu, France

[b] Institut Européen des Membranes, IEM, UMR-5635, ENSCM, CNRS, Univ Montpellier, Place Eugène Bataillon, 34095 Montpellier cedex 5, France

* Corresponding author: Tel +33 (0)4 68 30 77 30

E-mail address: stephane.abanades@promes.cnrs.fr

Abstract:

The investigation and optimization of solar fuels production by H_2O and CO_2 splitting reactions using non-stoichiometric redox materials as oxygen carriers relies on materials-related studies. The thermochemical cycles performance strongly rely on the thermodynamics and kinetics of redox reactions, as well as chemical composition and morphology of the reactive redox materials commonly based on ceria and perovskites. This study focusses on the evaluation and selection of suitable non-stoichiometric metal oxides for two-step thermochemical cycles with high fuel production yields, rapid reaction rates, and performance stability. The redox activities of different A- and B-site substituted perovskite materials (ABO_3) were experimentally investigated (with A=La, Sr, Y, Ca, Ce, Pr, Sm and B=Mn, Co, Fe, Mg, Al, Ga, Cr). The reactive powders were synthesized via modified Pechini methods providing a porous microstructure especially suitable for thermochemical cycles, while their redox activity was evaluated by thermogravimetric analysis. This experimental screening highlighted the difficulty to combine high reduction extent (δ) achievable by the reactive material with complete re-oxidation extent and fast reaction rates. From the redox activity study of manganite perovskites, $La_{0.5}Sr_{0.5}Mn_{0.9}Mg_{0.1}O_3$ (LSMMg) was pointed out as a good compromise between CO_2 splitting activity and thermal stability, possibly competing with ceria as a promising material for two-step thermochemical cycles. Both thermodynamic and kinetic studies were also performed to provide a better understanding of the mechanisms involved in thermochemical cycles. Thermodynamic properties derived from experimental $\delta(T,p_{O2})$ diagrams were used to predict the upper bounds for both reduction extent and fuel production performance at equilibrium. Regarding kinetics, the activation energy during LSMMg reduction was shown to increase with the increase of non-stoichiometry extent.

Keywords: Thermochemical redox splitting; Solar fuels; Ceramic materials; Perovskites; Ceria; CO_2 conversion; Hydrogen production.

1. Introduction

A main challenge for two-step thermochemical cycles is to develop a reactive material able to dissociate water and/or CO_2 with fast reaction rate and performance stability over cycles. Thus to be usable in solar-driven thermochemical cycles, a reactive material should satisfy most of the following criteria:

- favorable thermodynamics for low reduction temperature (<1400°C);
- capacity to produce high amounts of H_2 and/or CO during the oxidation step;
- fast kinetic rate;
- good thermal stability;
- low cost, non-toxicity, and largely available and abundant [1,2].

Typical redox-active materials used in thermochemical splitting are metal oxides based on either volatile (e.g. ZnO/Zn and SnO_2/SnO [3,4]) or non-volatile stoichiometric and non-stoichiometric redox pairs, involving spinel and fluorite-structured redox materials ($CeO_2/CeO_{2-\delta}$ [5,6], CeO_2/Ce_2O_3 [7], Fe_3O_4/FeO [8], ferrites [9–11], such as $NiFe_2O_4$ [12]). More exhaustive lists of relevant material formulations can be found in the literature [13–16]. Recently, non-stoichiometric ceramics with $ABO_{3-\delta}$ perovskite structure have attracted significant attention, thanks to their suitable redox properties, durability and reliability at high processing temperatures. More specifically, perovskite oxides arose as a promising class of materials for thermochemical cycles, due to the large range of reachable non-stoichiometry along with their stability over a large range of operating conditions. Unlike ceria, thermodynamics are not favorable to complete re-oxidation of perovskite materials, and either a large temperature swing between reduction and oxidation steps or an excess of oxidant is usually required to increase the fuel production rate [17]. However, the large amount of doping possibilities in perovskite materials offers great potential for tuning their thermodynamic properties. Perovskite formulations such as $La_{0.5}Ca_{0.5}MnO_3$ (LCM) and $La_{0.5}Sr_{0.5}MnO_3$ (LSM) with or without any dopant have been tested for either H_2O or CO_2 splitting [18–24]. Insertion of aluminum in B-site was found to increase both H_2 production and reaction kinetics, with stable production rate after 80 cycles [25]. The insertion of Ga in B-site (limited to 30% due to its low solubility) was found to increase the tolerance factor, with beneficial influence on the reduction rate [26]. Nair and Abanades [27] pointed out that Mg as dopant in B-site does not increase the fuel production rate but improves thermal stability. A detailed overview of the best performing perovskite formulations, with a special focus on their ability to produce solar fuel with high yield and stable performance was published by Haeussler et al. [15]. Doping strategies in perovskite materials represent a pathway to overpass the thermochemical performance of the current state-of-the-art ceria material. Broadly speaking, the search for performing reactive materials should aim to decrease the reduction temperature and the temperature swing between steps, while optimizing the reduction and re-oxidation extents and enhancing the kinetics. However, a trade-off between reduction and re-oxidation performance is usually necessary. Other important criteria include non-toxicity, availability of the resource and environmental impact of material production/shaping. Other tools such as density functional theory can be useful to orient the choice of oxygen carriers. A detailed experimental study is also required to select the reactive materials and validate their applicability for thermochemical cycles. In light of the available data on the redox materials investigated so far, the most promising compositions were selected to study experimentally their redox activity.

This study aims to present an experimental screening of promising materials compositions in order to identify suitable redox systems for thermochemical cycles. First, the impact of various dopants on thermochemical performance has been investigated on a series of powders prepared by Pechini-derived synthesis methods. The investigated materials encompass Ca and Sr-based lanthanum-manganese perovskites, Sm and Pr-based strontium-manganese perovskites, lanthanum-cobalt perovskites, yttrium-manganese perovskites, barium-manganese perovskites, and ceria-based oxides. The redox behavior of the powders was studied in two-step cycles. The purpose was both to investigate new formulations and to corroborate (or invalidate) results reported by other studies on whether the dopants do enhance the thermochemical performance of the considered perovskites. The most promising materials were finally selected to perform thermodynamic and kinetic studies based on thermogravimetric analyses in order to provide better understanding of the mechanisms involved in thermochemical cycles. The thermodynamic analysis was used to predict the theoretical performance of the oxygen carrier materials and can be wisely applied to pre-select potential reactive materials. Such a thermodynamic study does not include practical considerations such as kinetic limitations or sintering effects. It was thus completed by a kinetic study. The latter provided essential information and better understanding about reaction mechanisms and durations, which are key parameters for reactor design and large-scale implementation. In this work, the kinetic and thermodynamic characteristics of redox reactions were extensively probed. Both $Ca_{0.5}Sr_{0.5}MnO_3$ (CSM) and $La_{0.5}Sr_{0.5}Mn_{0.9}Mg_{0.1}O_3$ (LSMMg) were selected as benchmark materials to illustrate the thermodynamic equilibrium approach. CSM was previously considered as a ceria membrane coating to boost oxygen exchange [28], while LSMMg was used to promote fuel production capacity of ceria foams [29]. The kinetic study of LSMMg further revealed an evolution of the activation energy as a function of the reduction extent during the reduction reaction, which was never investigated before.

2. Materials and method

2.1. Materials synthesis

The perovskite powders were synthesized by Pechini-derived methods [30,31] based on the utilization of nitrate metal salts (M), citric acid (CA) as a chelating agent, and ethylene glycol (EG) as a complexing agent. Two different solution formulations with the following molar ratios: M:CA:EG=1:1.5:1 (P1 method) and M:CA:EG=1:5:20 (P2 method) have been applied. In a typical synthesis, the given quantity of metal nitrates was dissolved in water with the fixed M:H_2O mass ratio of 1:6.

LSM powders (with or without Mg or Al dopant) were first prepared by the P1 method. The mixture of nitrate salts and CA (CA:M=1.5:1) was heated to 60°C and stirred for 10 min. Then, EG was added to the solution with the molar ratio EG:CA=0.66:1.

In parallel, LSM and LCM powders were prepared by P2 method, in which large excess of CA was added to the metal salts solution (CA:M=5:1). The mixture was heated to 60°C and stirred for 10 min. Then, a large excess of EG was added to the solution with the molar ratio EG:CA=4:1. It was highlighted [24] that large excess in citrate agent (P2-method) leads to increased powder sinterability, which can be suitable to realize dense layers. In contrast, the P1-method was found relevant to synthesize reactive materials with low sinterability, yielding stable performance in thermochemical two-step cycles.

For both methods, the final mixture was heated to 120°C until a viscous colored sol was obtained, which was further heated to 250°C for 2 h to form a polymeric resin (polyesterification step). The as-obtained resin was crushed using an agate mortar and subsequently treated in successive thermal treatment steps in air atmosphere: i) 600°C for 1 h with a 3°C/min ramp yielding a porous ceramic powder, ii) 1400°C for 1 h with a 5°C/min ramp, yielding the final perovskite material which was used in two step thermochemical CO_2 splitting reactions. All sample references, corresponding formulations, and synthesis methods are reported in Table S1.

2.2. Characterization methods

The main physico-chemical characteristics (morphology, chemical composition, crystalline structure, and microstructure) of the P1 and P2 powders have been determined and compared. The powders morphology and grain sizes were observed by Field Emission Scanning Electron Microscopy (FESEM – Hitachi S4800).

The crystallographic structure of the investigated powders was analyzed at room temperature by X-ray diffraction (XRD) using a PANalytical XPert Pro diffractometer (Cu Kα radiation, $\lambda = 0.15418$ nm). A 20-75° angular range was used with θ-θ symmetrical scan. X-ray diffractograms were recorded and analysed with PANalytical softwares (Data collector and HighScorePlus). All the collected XRD patterns are presented in Supporting Information.

Particle size distributions were measured by laser diffraction (Mastersizer 3000) coupled with a fluid dispersion system (Hydro EV). The system was operated at two wavelengths (633 nm and 470 nm). Ultrasounds were used to operate powder dispersion in water and particle size distribution was determined by applying the Fraunhofer diffraction theory [32].

The thermochemical CO_2 splitting reactivity of the powders prepared at 1400°C was studied via thermogravimetric analysis (TGA – SETARAM SETSYS) using a platinum crucible. Around 100 mg of powders was used for each TGA experiment. The temperature was first increased to 1400°C (20°C/min) under argon (99.999% purity, < 2 ppm of O_2, 0.020 NL/min) to perform the thermal reduction. After 45 min plateau at 1400°C, the temperature was decreased to 1050°C (20°C/min). A mixture of CO_2 and Ar (1:1) was then introduced (0.010 NL/min for each) in the system to perform the oxidation step, during 60 min. Then the temperature was increased again to 1400°C under argon, and the thermal reduction and CO_2 splitting reaction cycle was operated again. The mass variation due to oxygen release during the thermal reduction step and oxygen uptake during CO_2 splitting step was recorded continuously, and the amounts of O_2 and CO produced were calculated [23]. Specific H_2O splitting tests were also performed in a tubular furnace with online O_2 and H_2 analysis (Figure S1).

For the thermodynamic study, different temperature dwells (ranging from 1000 to 1400°C) were carried out in TGA at different oxygen partial pressures (from 10 to 10000 ppm) to determine the $\delta(T,p_{O2})$ diagrams. Regarding kinetic analysis, the reduction in Ar up to 1400°C was carried out under different heating rates (non-isothermal tests) to determine both the conversion rate and δ values as a function of the temperature.

3. Results and discussion

3.1. Influence of chemical composition and dopants on the redox activity

A series of promising materials and dopants was investigated for thermochemical cycles application. All the selected reactive compositions are reported in Table S1, along with their abbreviations. The selected material compositions were synthesized with a modified Pechini method, and their crystallographic structure was determined by XRD analysis. The redox behavior of powder series was investigated via TGA (gas yields are reported in Table S2), and their structural stability was assessed via XRD analysis after thermochemical cycles, in order to detect any evolution of crystallographic phases. SEM was also applied to analyze the microstructure of powders and their morphological evolution. Finally, the most promising formulations were selected for further thermodynamic and kinetic studies.

3.1.1. Ca and Sr-based lanthanum manganese perovskites (A- and B-sites substituted)

Lanthanum manganite perovskites have been investigated for numerous applications such as electrodes in solid oxide fuel cells [33], metal-air batteries [34], gas and ion sensors [35,36] or high performance materials for catalysis [37]. Addition of Ca has been considered to achieve high reduction extent [21,22]. Lanthanum-strontium manganite perovskites have been investigated for applications in microelectrodes [38]. For two-step thermochemical cycles, Sr-based and Ca-based lanthanum manganite perovskites have been widely studied [39]. However, their low re-oxidation extent is an issue. Thus, to enhance the thermochemical performance, different dopants were selected on the basis of their promising behavior reported in the literature: Al, Cr, Ga, and Mg. The following perovskites were investigated in this work: $La_{0.5}A_{0.5}Mn_{0.6}Al_{0.4}O_3$, $La_{0.5}A_{0.5}Mn_{0.6}Cr_{0.4}O_3$, $La_{0.5}A_{0.5}Mn_{0.6}Al_{0.2}Cr_{0.2}O_3$, $La_{0.5}A_{0.5}Mn_{0.8}Ga_{0.2}O_3$, and $La_{0.5}A_{0.5}Mn_{0.9}Mg_{0.1}O_3$. The $La_{0.5}A_{0.5}MnO_3$ materials were used as references (with A=Sr, Ca). A comparative study was performed to elucidate the influence of the modified-Pechini method parameters and of the dopants on the reactivity of the derived powders. The crystallographic structure of the considered material series was studied by XRD analysis (Figures S2-S3). All the LSM powders exhibit a cubic phase, with lattice parameter a in the range 3.840-3.864 Å.

The LCM powders exhibit an orthorhombic phase with lattice parameter *a* in the range 5.346-5.431 Å, *b* in the range 5.362-5.432 Å, and *c* in the range 7.593-7.688 Å.

In a previous work [24], the characteristics of powders prepared by P1 and P2 modified-Pechini methods were investigated to select the most adapted protocols yielding perovskite formulations and microstructures with both suitable sinterability (depending on the targeted application involving either porous microstructures or densified membranes) and attractive CO_2 splitting performance. Dilatometric results clearly evidenced that P1-powders offer low sinterability and densification below 1400°C, whereas P2-powders show enhanced sintering at this point [24]. The P2 powders were easily shaped as pellets and their sintering was controllable up to strong densification at about 1400°C. In contrast, the P1 powders were found to present heterogeneities and a spongy microstructure due to combustion reactions during their synthesis [40].

A comparison of the redox activity of both P1 and P2-powders (LSM, LSMMg and LSMAl) for CO_2 splitting reaction reveals similar fuel production yield during two-step thermochemical cycles (Table S2). The highest CO amount (215-217 µmol/g) is produced by LSMMg with an almost complete re-oxidation yield for both P1 and P2 powders (97%), thereby confirming cycling stability. For all samples, the CO production yield during the first and second cycles is similar.

Figure 1 compares the O_2 and CO production yields obtained from TGA for the series of Sr and Ca-based perovskites (data from [24]). The reduction extent reached during the first cycle is enhanced by Al^{3+} and Mg^{2+} dopants in comparison with LSM and LCM reference perovskites. On the contrary, the reduction step is not improved by Ga^{3+} and Al/Cr dopants and the Cr dopant is even unfavorable. The O_2 production starts at 800°C for all the Sr-based perovskite series, against 900°C for the Ca-based perovskites, except for LCMAl with a start at 650°C unveiling a lower reduction enthalpy. This explains the higher reduction extent reached by LCMAl in comparison with other Ca-based perovskites.

Concerning the oxidation step of Ca-based perovskites, only LCMGa offers higher CO production yield in comparison with LCM, but re-oxidation extent is low (below 60%). The other dopants (Al, Cr, and Mg) negatively impact the amount of CO produced. For Sr-based perovskites, the Mg^{2+}, Ga^{3+} and Al^{3+} dopants lead to an enhancement of the CO production yield in comparison with LSM. The CO production yields obtained during the first and the second cycles are similar, confirming the thermochemical stability of the perovskite series. The re-oxidation extents reached during the second cycles are above 90% except for Al/Cr that only reaches 83% due to its low CO production yield. Therefore, apart from Cr and Cr/Al^{3+} dopants, Ga^{3+}, Al^{3+} and Mg^{2+} are able to enhance LSM performance. In this series, LSMMg seems to be the most promising material since it offers both the highest CO production yield and enhanced performance stability.

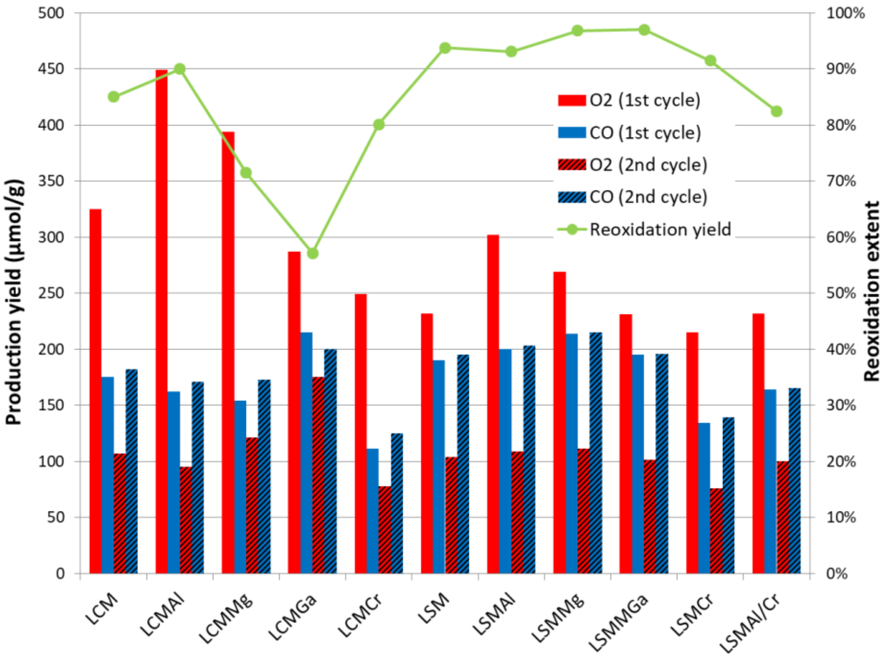

Figure 1: Influence of dopants on O_2 and CO production yields, and re-oxidation extent (2nd cycle) for series of Ca and Sr-based perovskites

TGA thus points out the promising redox behavior of LSMMg. In order to further provide insights into the thermochemical reactions of LSMMg, two thermochemical H_2O splitting cycles were carried out in an electric tubular furnace (Figure S1), with ~0.8 g of reactive material. The system permits to directly analyze the O_2 and H_2 gas produced at the outlet, thus yielding production rate values (Figure 2). The reduction step was performed at 1400°C after a heating ramp of 10°C/min, with an Ar flow rate of 0.2 L/min. The oxidation step was performed at 1050°C for 40 min under 50% of H_2O. The O_2 and H_2 production yields obtained with the tubular furnace were in the same order of magnitude than the O_2 and CO production yields measured by TGA (207 µmol/g against 269 µmol/g for O_2, and 236 µmol/g for H_2 against 215 µmol/g for CO, in tubular furnace and TGA, respectively). In the 2nd cycle, O_2 and H_2 yields were 123 and 251 µmol/g, confirming complete re-oxidation. The oxygen production rate increased with the increase of temperature and reached a peak value at the target temperature. Then, the O_2 production decreased slowly until reaching a sufficiently low production rate value and the temperature was then decreased for the oxidation step. The H_2 production rate reached a peak few seconds after steam injection and then slowly decreased. This fits the kinetic studies reported for perovskites in the literature [18,41]. The H_2 production rate reached a maximum value of 0.31 mL/min/g during both cycles, denoting good production stability for LSMMg-P1. These results demonstrate that LSMMg is able to split both CO_2 and H_2O with similar performance.

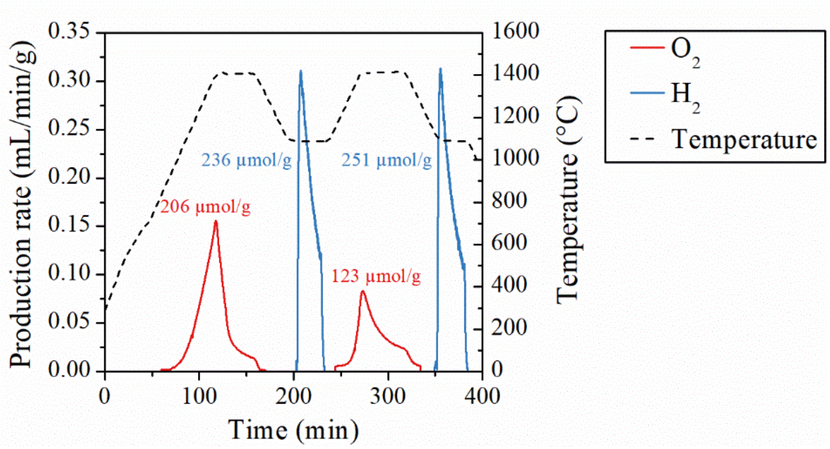

Figure 2: O_2 and H_2 production rates during two consecutive thermochemical cycles for H_2O splitting, performed in a tubular furnace with LSMMg-P1

To explain the good thermochemical performance of LSMMg-P1, its microstructure was observed by FESEM. Figure 3 presents the micrographs of LSMMg-P1 powder before and after redox cycles in TGA. The spongy microstructure results from nitrate decomposition during Pechini synthesis. Such a morphology is typical for powders obtained by combustion reactions [40]. Grain sizes were measured in the range 0.5-1 µm. Furthermore, the two thermochemical cycles performed during TGA did not induce any sintering, as confirmed by the limited grain growth. The presence of Mg^{2+} ion as stabilizer in the perovskite structure could explain this behavior. Indeed the strong Mg-O bond, resulting in high melting temperature for MgO (2800°C), could explain its good thermal resistance [20]. Thermal resistance is a key asset for further process implementation, as the reactive material should undergo multiple cycles while maintaining stable performance. Thus, LSMMg-P1 appears as a promising candidate for this purpose.

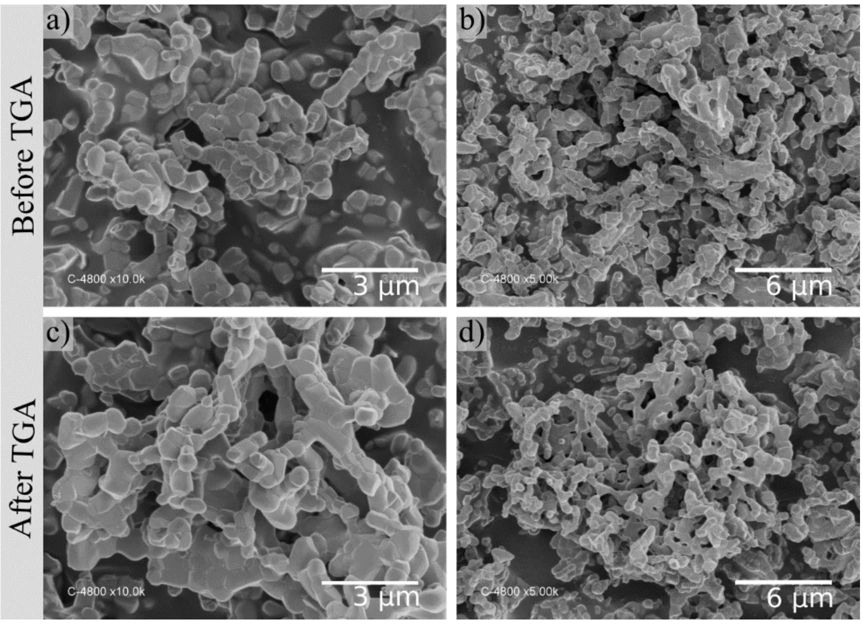

Figure 3: FESEM observations of LSMMg-P1 powder: a) and b) before cycling; c) and d) after cycling in TGA for CO_2 splitting

The grain size distribution is another important characteristic of the reactive powder, with direct influence on its specific surface area. Indeed, a high specific surface area promotes production rate during the surface-controlled oxidation step. The particle size distribution of both fresh and cycled LSMMg-P1 powders was investigated by laser diffraction (Figure 4), using the Fraunhofer diffraction theory and the assumption of spherical particles. For the fresh sample, a bimodal distribution of particle sizes is observed with two maximums centered at 5.9 µm and 27.4 µm. After two thermochemical cycles in TGA (CO_2 splitting), the proportion of small particles strongly decreased in favor of larger ones, attributed to slight sintering effect. The two initial distributions shift, combine, and form a single distribution, centered at 40.1 µm. In comparison with the small grain sizes (0.5-1 µm) observed by SEM [24], the large particle sizes measured by laser diffraction correspond to consolidated aggregates of grains partially sintered. It appears clearly in Figure 3 that these porous aggregates are more efficiently consolidated (sintered) after cycling although the size of grains within the aggregates remains almost unchanged.

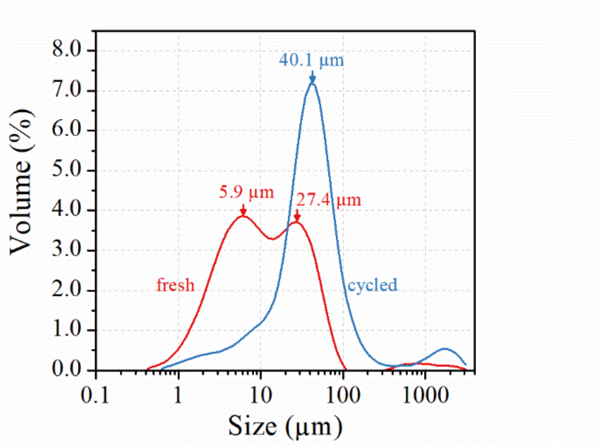

Figure 4: Particle size distribution of fresh (red) and cycled (blue) LSMMg-P1 powder

To sum up, Ca-doped perovskites offer higher reduction extent than Sr-doped perovskites. Conversely, Sr-based perovskites show higher re-oxidation yield than Ca-based perovskites. The use of Mg dopant in B-site is promising. Mg^{2+} is not involved in redox reactions but it enhances the oxidation degree of Mn (compared with Ga^{3+} and Al^{3+}), thus favoring both reduction and oxidation extents. Mg^{2+} also acts as a sintering inhibitor as the LSMMg powder remains well dispersed and not cohesive after TGA cycling, whereas other powders tend to sinter.

3.1.2. Sm and Pr-based strontium manganese perovskites

Numerous studies have investigated perovskites with lanthanum in the A-site. In this work, other rare earth elements such as samarium or praseodymium were investigated instead of lanthanum in order to promote thermochemical performance. Five compositions were selected: $Sm_{0.75}Sr_{0.25}MnO_3$ (SmSrM75), $Sm_{0.5}Sr_{0.5}MnO_3$ (SmSrM50), $Pr_{0.75}Sr_{0.25}MnO_3$ (PrSrM75), $Pr_{0.5}Sr_{0.5}MnO_3$ (PrSrM50) and $Pr_{0.25}Sr_{075}MnO_3$ (PrSrM25). The P1 method was used to synthesize the powder series. Their crystallographic structures were studied by XRD (Figure S4). It should be noted that the synthesis of $Sm_{0.25}Sr_{0.75}MnO_3$ formulation was also attempted, but XRD analysis showed that the perovskite structure did not form.

Figure 5 shows TGA results for the strontium-manganese perovskite series (including LSM for comparison). First, the Sr content influences the non-stoichiometry extent reached by the reactive material. A high Sr content induces a high amount of oxygen released; for example PrSrM25 ($Pr_{0.25}Sr_{075}MnO_3$) produces 668 µmol/g of O_2 against 146 µmol/g for PrSrM75 ($Pr_{0.75}Sr_{0.25}MnO_3$). The O_2 production rate is also sharply enhanced (Figure S5). As highlighted in the literature, increasing the Sr content increases the Mn oxidation state in B-site. As the reduction reaction depends on the reduction of Mn^{4+} to Mn^{3+}, an increase of Sr content enhances the reduction extent [18,39,42–47]. However, increasing Sr content does not enhance the CO yield. For a fixed Sr content, the amount of O_2 released depends on the Sr-substitution element in the A-site. With 50% Sr, the O_2 production yield increases in the following order: LSM (232 µmol) < PrSrM50 (268 µmol/g) < SmSrM50 (377 µmol/g). Using Sm^{3+} or Pr^{3+} in the A-site thus enhances the reduction step in comparison with La^{3+}. The CO production during the first cycle increases in the following order: PrSrM50 (153 µmol/g) < SmSrM50 (169 µmol/g) < LSM (190 µmol/g). The highest O_2 production yield is obtained with PrSrM25 (668 µmol/g) whereas the highest CO production yield is obtained with SmSrM75 (180 µmol/g). Thus, Sm and Pr in A-site (instead of La) have beneficial impact on the reduction step but they decrease the amount of CO produced during the oxidation step, impeding the enhancement of thermochemical performance. However, all the materials show very good fuel production stability and higher productivity than pure ceria under similar conditions [48].

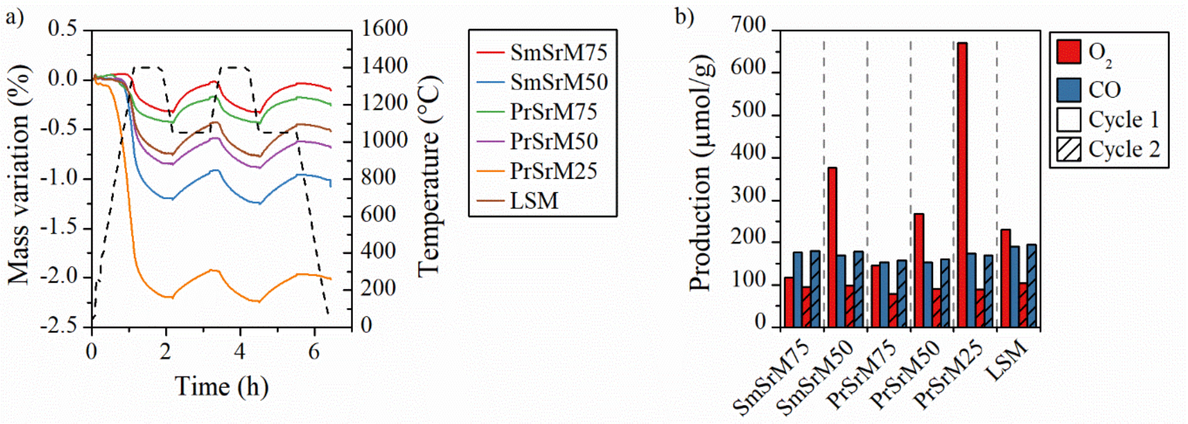

Figure 5: a) Thermogravimetric reduction and re-oxidation profiles for CO_2 splitting and b) O_2 and CO production yields for a series of strontium manganite perovskites

3.1.3. Lanthanum cobalt perovskites

Lanthanum cobalt perovskites were studied for their attractive magnetic properties [49] or their performance as cathode materials in high temperature fuel cells [50]. Due to their high oxygen exchange capacities, lanthanum cobalt perovskites also appear as potentially attractive reactive materials for thermochemical cycles. Both $La_{0.5}Sr_{0.5}CoO_3$ (LSCo) and $LaMn_{0.5}Co_{0.5}O_3$ (LMCo) were selected for tests in thermochemical cycles. The XRD patterns of LSCo and LMCo confirm the formation of the expected crystallographic structure (Figure S6). Figure S7 compares the mass variation during two thermochemical cycles for LSCo and LMCo. The LSCo cycles were carried at a lower reduction temperature (1300°C) due to the melting risk of this material at higher temperatures. The oxidation temperature was also decreased to 950°C in order to maintain a similar temperature swing for all TGA cycling experiments. The CO production yield of LMCo was low (~100 µmol/g) due to the weak non-stoichiometry extent reached during the reduction step ($\delta=0.021$). On the contrary, LSCo reached a high reduction extent during the first cycle (1191 µmol/g) and high subsequent mass uptake (1141 µmol/g) despite a low re-oxidation extent (48%). This result was ascribed to carbonate formation, as denoted by the sharp mass loss observed when stopping CO_2 feed (also evidenced in [23]), reflecting prompt decarbonation (CO_2 release) and unsuitability for CO_2 redox splitting. In a previous work in our group, this material was also tested for H_2O splitting and low H_2 production was measured, confirming its low thermochemical splitting activity [43]. In addition, strong sintering or partial melting occurred in the crucible after TGA performed with CO_2. The XRD pattern of LSCo after thermochemical cycles highlighted the decomposition of $La_{0.5}Sr_{0.5}CoO_3$ to $LaSrCoO_4$ and CoO (Figure S6), as previously pointed out in [43].

3.1.4. Yttrium manganese perovskites

Yttrium manganese perovskites have been widely studied for air separation applications due to their ability to selectively absorb, store and release significant amounts of oxygen [51]. The high oxygen exchange capacity is a key parameter for reactive materials in thermochemical cycles. In this respect, series of yttrium manganese perovskites were investigated in this work for thermochemical CO_2 splitting cycles. Four promising compositions were selected: $Y_{0.97}La_{0.03}MnO_3$ (YLaM), $Y_{0.9}Ce_{0.1}MnO_3$

(YCeM), $Y_{0.87}Sr_{0.1}La_{0.03}MnO_3$ (YLaSrM), and $Y_{0.9}Sr_{0.1}MnO_3$ (YSrM). The XRD patterns of the prepared yttrium-manganite perovskite series are shown in Figure S8. Their structures correspond to the space group P63cm (01-070-4962). YSrM shows a peak shift due to the substitution of Y^{3+} by Sr^{2+} in comparison with $YMnO_3$, inducing the following lattice parameters: a=6.11 Å and c=11.25 Å. After thermochemical cycles, the lattice parameters slightly increase, with a=6.16 Å and c=11.47 Å. Both YLaM and YCeM show increased lattice parameters (a=6.16 Å and 6.21 Å; c=11.48 Å and 11.98 Å, respectively) in comparison with $YMnO_3$ (a=6.13 Å; c=11.40 Å). This is due to the higher ionic radii of La (1.03 Å) and Ce (1.01 Å) in comparison with Y (0.90 Å) [52]. Similarly to YSrM, both YLaM and YCeM present a decrease in lattice parameters after thermochemical cycles: a=6.15 Å and c=11.43 Å for YLaM and a=6.20 Å and c=11.94 Å for YCeM.

Figure 6 shows the mass variation during two thermochemical cycles, along with the O_2 and CO production yields. The TGA of YCeM was aborted after the first cycle due to very low re-oxidation extent. A high mass loss was observed during the first part of the reduction step (until 1128°C) and thus, only the mass variation measured during the second part of the reduction step (above 1128°C) was taken into account to calculate the oxygen yield. Among the tested yttrium manganese perovskites, YLaSrM reached the highest reduction extent with 145 µmol/g of O_2 in comparison with 54 µmol/g, 47 µmol/g, and 127 µmol/g for YLaM, YCeM, and YSrM, respectively. The CO production yields follow the same trend as the O_2 production yields, suggesting that CO production depends on the achieved non-stoichiometry, with the following yields: YLaSrM (135 µmol/g) > YSrM (118 µmol/g) > YLaM (86 µmol/g) > YCeM (33 µmol/g). Despite its low reduction extent, YLaM displays high re-oxidation extent (77%) during the 1st cycle in comparison with YSrM (46%). Furthermore, both O_2 and CO production yields for YSrM during the 2nd cycle are lower (106 µmol/g and 106 µmol/g, respectively) than those of the first cycle (127 µmol/g and 118 µmol/g, respectively). On the contrary, YLaM exhibits an increase of both O_2 and CO production yields when comparing the first and second cycles (from 54 to 60 µmol/g and from 86 to 107 µmol/g, respectively). This can be explained by a slow reduction rate of the material. Indeed during the first cycle, YLaM does not reach its maximum reduction extent. So, the non-stoichiometry extent continues to increase during the second step. Among the yttrium manganese perovskites investigated, YLaSrM offers the best performance with the highest CO production yield (137 μmol/g). Furthermore, the CO production yield is stable between the first and the second cycle, highlighting the thermochemical stability of this perovskite material. The re-oxidation extent of YLaSrM during the second cycle reached 91%. Consequently, YLaSrM appears as the most promising reactive material among the investigated yttrium manganese perovskite series.

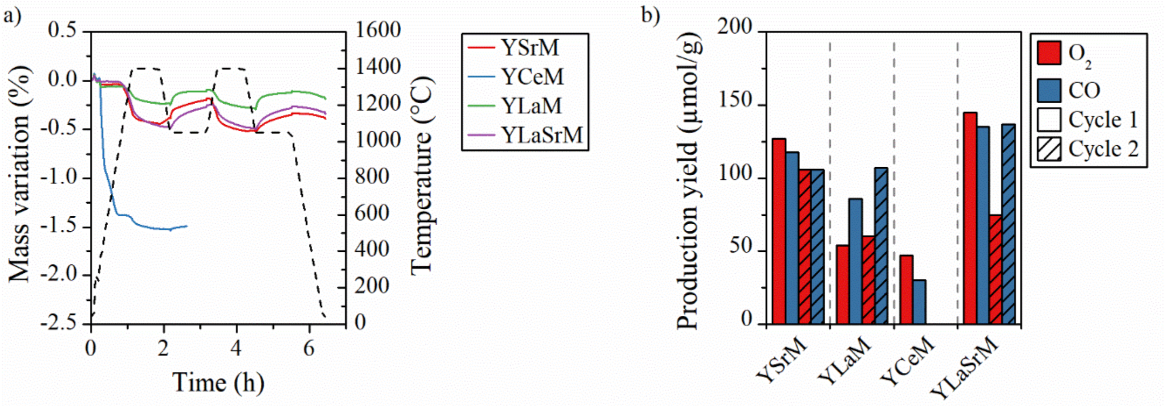

Figure 6: a) Thermogravimetric reduction and re-oxidation profiles with CO_2 (solid lines) and associated temperatures (dashed lines), b) O_2 and CO production yields for yttrium manganite perovskite series

3.1.5. Barium manganese perovskites

Barcellos et al. identified cerium-doped barium manganese perovskite as a promising water-splitting material due to its appropriate oxygen bonding strength [53]. In order to test this type of perovskite, $BaCe_{0.5}Mn_{0.5}O_3$ (BaCeMn) was synthesized by the Pechini method. As reported in [53], a mixture of two phases $BaCe_{0.5}Mn_{0.5}O_3$ and CeO_2 was evidenced in the XRD patterns (Figure S9). Two TGA cycles were carried out as presented in Figure S10. During the first cycle, 220 μmol/g and 154 μmol/g of O_2 and CO were produced, respectively. These values are in line with those obtained for lanthanum manganese perovskites [39]. However, during the second cycle, CO production yield fell to 110 μmol/g and a poor re-oxidation yield was achieved. Such a decrease in performance is not consistent with the good stability highlighted by Barcellos et al. [53]. This may be explained by the slightly higher reduction temperature used here (1400°C) in comparison with Barcellos work (1350°C). Indeed higher temperatures can induce sintering that could hinder the re-oxidation reaction. Furthermore, a decomposition of the BaCeMn structure (with formation of $BaCeO_3$ and MnO_3 phases) was evidenced by XRD after cycling (Figure S9), thus explaining the degradation of thermochemical performance. For these reasons, such a formulation appears unsuitable for solar thermochemical application.

3.1.6. Ceria and doped-ceria

Currently, ceria is considered as the state-of-art material for two-step thermochemical cycles, due to the stability of its crystallographic structure over a large range of non-stoichiometry and working conditions. However, it suffers from a low reduction extent impeding high fuel production yield [54–57]. Numerous doping strategies have been explored to improve ceria thermochemical performance [48,58–60]. In this work, three promising compositions were selected from the literature and synthesized via Pechini method (P2): $Ce_{0.85}Zr_{0.15}O_2$ (CeZr15), $Ce_{0.63}Zr_{0.37}O_2$ (CeZr37) and $Ce_{0.63}Zr_{0.27}Al_{0.1}O_2$ (CeZr27Al10). CeO_2 was used as reference material. The formation of a fluorite structure was checked by XRD for all the selected formulations (Figure S11). Figure 7 shows the TGA profiles of both ceria and doped-ceria powders along with the O_2 and CO production yields. In comparison with pure ceria, the doped-ceria series present enhanced reduction extent during the first cycle (in the range of 116-176 µmol/g compared with 55 µmol/g for pristine ceria). Doping with Zr has a beneficial impact on ceria reduction extent: the reduction extent increases from 55 µmol/g for pure ceria to 176 µmol/g for CeZr37. The lattice distortion induced by the incorporation of Zr^{4+} enhances oxygen mobility, explaining the high O_2 yield obtained with Zr-doped ceria [60,61].

The total amount of dopant in CeZr27Al10 and CeZr37 is similar (37%), however the O_2 released by CeZr27Al10 (129 µmol/g) is significantly lower than the value measured for CeZr37 (176 µmol/g). Thus, simultaneous incorporation of both Al and Zr into ceria is not beneficial to the reduction extent. Concerning the oxidation step, the CO production yield increases in the following order: CeZr37 (72 µmol/g) < CeO_2 (95 µmol/g) ≈ CeZr27Al10 (86 µmol/g) < CeZr15 (144 µmol/g). Doped-ceria materials offer low re-oxidation extent (in the range of 20-62%) in comparison with pristine ceria (77%) due to slow kinetics. During the second cycle, CeZr37 and CeZr27Al10 show a decrease of the amount of CO produced (69 µmol/g and 57 µmol/g, respectively) in comparison with the first cycle (72 µmol/g and 86 µmol/g, respectively). Such decrease in performance is attributed to the low thermal stability of the microstructure of these materials (synthesized via P2 method, favoring strong sintering and well adapted for preparing dense membrane [24]), making them not suitable for consecutive cycling operation. Within this series, the best performing materials are thus pure ceria due to high re-oxidation rates, and CeZr15 due to the improved fuel productivity (at the expense of lowered oxidation rates for Zr-substituted ceria). When considering two-step redox cycles, the activity of ceria and ceria-zirconia synthesized via different methods was studied before [62]. The thermal stability of the microstructure of these ceria-based materials was enhanced when adequate synthesis methods were used to limit sintering, thus enhancing final CO production yields. However, the fuel yield relative to unit mass of ceria remains low because the reduction extent (δ value) is limited, and most of perovkite formulations compete favorably with ceria in terms of reduction extent and fuel productivity.

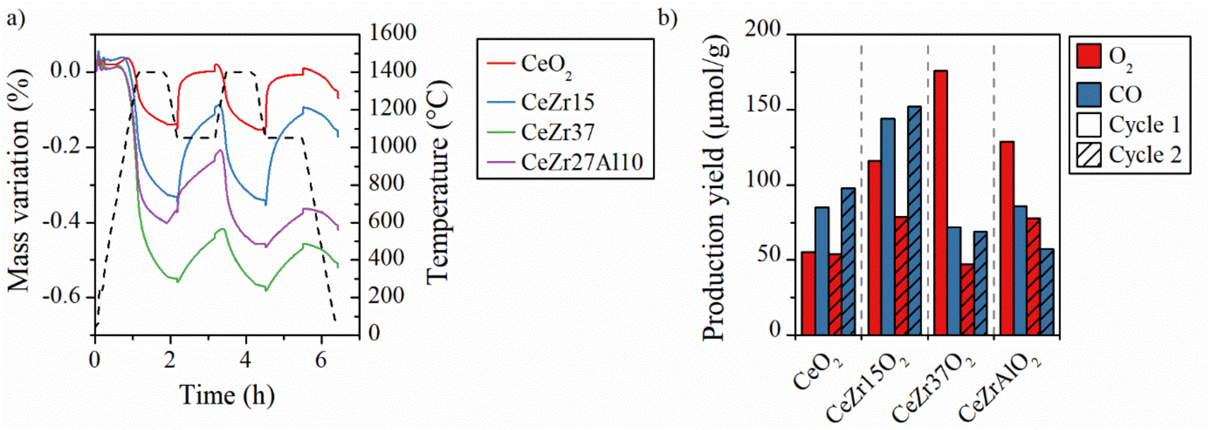

Figure 7: a) Thermogravimetric reduction and re-oxidation profiles (solid lines) with associated temperatures (dashed lines), b) O_2 and CO production yields for ceria and doped-ceria materials

3.2. Thermodynamic study

The determination of thermodynamic properties is interesting to predict both the theoretical reduction extent and the fuel production yield of materials. Thermodynamic properties were assessed from experimental measurements of oxygen non-stoichiometry δ at given T-pO_2, for two selected materials: LSMMg-P1 (the most promising material studied here) and $Ca_{0.5}Sr_{0.5}MnO_3$ (CSM).

The CSM perovskite was already studied for thermochemical energy storage applications due to its excellent oxygen exchange capacity and associated heat storage capacity [63,64]. However, a re-oxidation with CO_2 at 1050°C is unsuitable to observe significant CO production. A re-oxidation performed during continuous temperature decrease revealed that the oxidation rate became more favorable when approaching 600°C. After a reduction at 1400°C under 10 ppm O_2, the final non-stoichiometry extent reached by CSM near equilibrium led to an O_2 production yield of 1302 µmol/g (Figure 8.a). After cooling down to 600°C in Ar, followed by CO_2 injection (50%), its re-oxidation extent was weak (less than 20%), which highlights the need for a large temperature swing to favor the oxidation step and produce significant amounts of CO (~350 µmol/g at 600°C after a reduction plateau up to 1400°C for CSM, Fig. 8a). Similarly, $Ca_{0.5}Sr_{0.5}Mn_{0.5}Fe_{0.5}O_3$ (CSMF) displays an O_2 yield of 913 µmol/g at 1300°C under 10 ppm O_2 and a CO production yield of 315 µmol/g at 600°C (Figure S12). For such perovskites, a large temperature swing is thus required for acceptable CO production, which is inappropriate for rapid cycling due to the required heating/cooling stages between reaction steps of thermochemical cycles. These results evidence very different redox behaviors for CSM and LSMMg materials and it was particularly relevant to study and compare their thermodynamic properties.

To evaluate the partial molar enthalpy and entropy as a function of the non-stoichiometry, the Van't Hoff method was applied according to Equation (1) [65,66]. If $\Delta H°(\delta)$ and $\Delta S°(\delta)$ do not depend on the temperature, as often observed, an Arrhenius plot of a set of T-pO_2 pairs for a given δ value yields a linear curve, with the values of enthalpy and entropy of reduction given by the curve slope and intercept, respectively. To this aim, three steps are required, as represented in Figure 8 for CSM material. Firstly, thermogravimetric analyses were carried out with temperature steps (1000°C, 1100°C, 1200°C, 1300°C, and 1400°C) under different values of oxygen partial pressures p_{O_2} (10 ppm, 250 ppm, 2000 ppm, and 10000 ppm). Figure 8.a and 8.b present the thermogravimetric analysis of CSM under 10 ppm O_2 and 250 ppm O_2, respectively. At the different temperatures, for all the couples $(T,\ p_{O_2})$, the non-stoichiometry at equilibrium δ was determined (by numerical extrapolation for low p_{O2} conditions because equilibrium is often hardly reached for the lowest p_{O2} value corresponding to 10 ppm). Secondly, for all the investigated p_{O_2} values, the non-stoichiometry extent δ was plotted as a function of temperature, as shown in Figure 8c. Finally, for each δ value, the logarithm plot of p_{O_2} versus the inverse temperature was fitted by linear regression from which the enthalpy and entropy of reduction were extracted using Eq. (1) (Figure 8d). Thus, both enthalpy and entropy can be calculated for all the non-stoichiometry extent values. Likewise, the different data used to compute the thermodynamic properties of LSMMg are presented in Figure 9.

$$\ln\left(\frac{p_{O_2}}{P^\circ}\right)_\delta = \frac{2\Delta S_o(\delta)}{R} - \frac{2\Delta H_o(\delta)}{RT} \qquad (1)$$

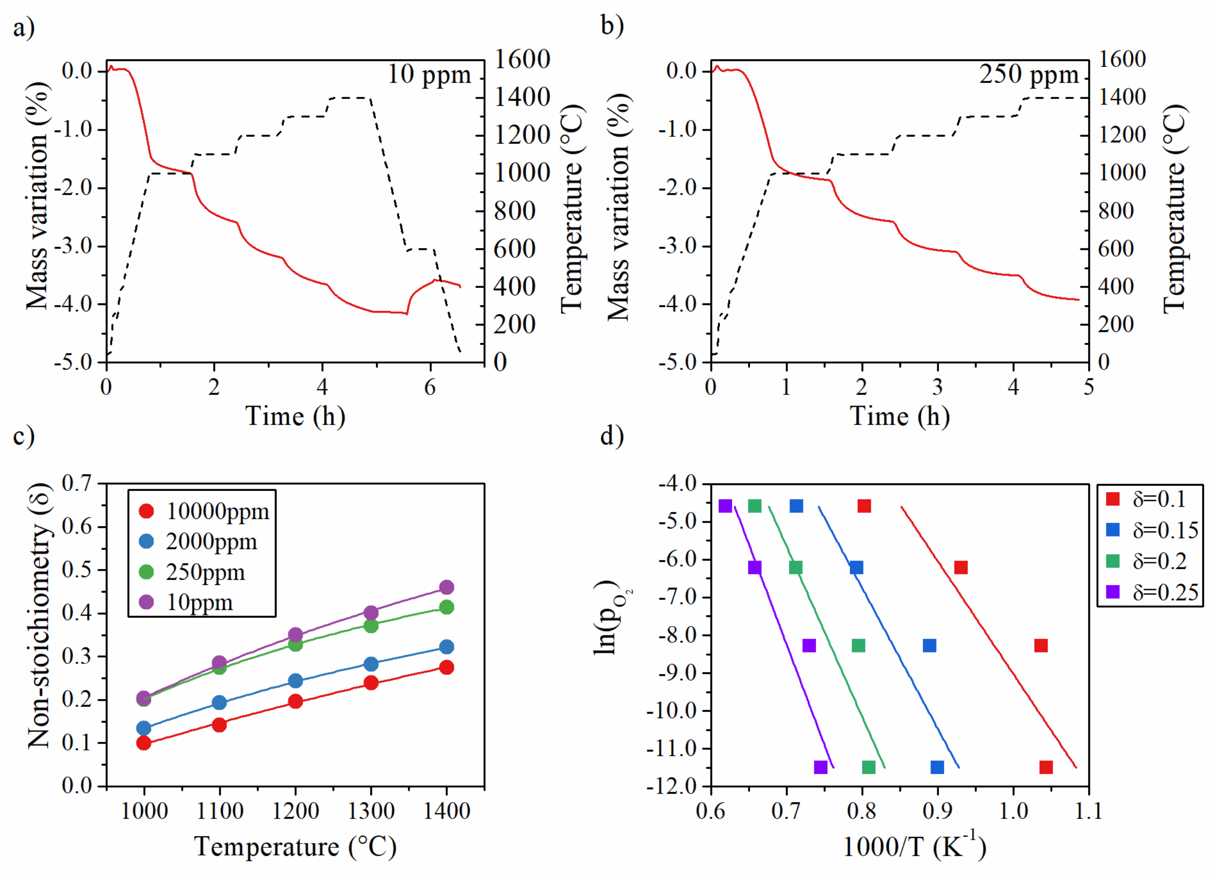

Figure 8: a) TGA of CSM under 10 ppm O_2 and b) TGA of CSM under 250 ppm O_2, with successive temperature steps (heating rate of 20°C/min, dwell of 45 min at each temperature plateau), c) non-stoichiometry extent as a function of temperature, and d) logarithm of oxygen partial pressure versus inverse temperature for CSM

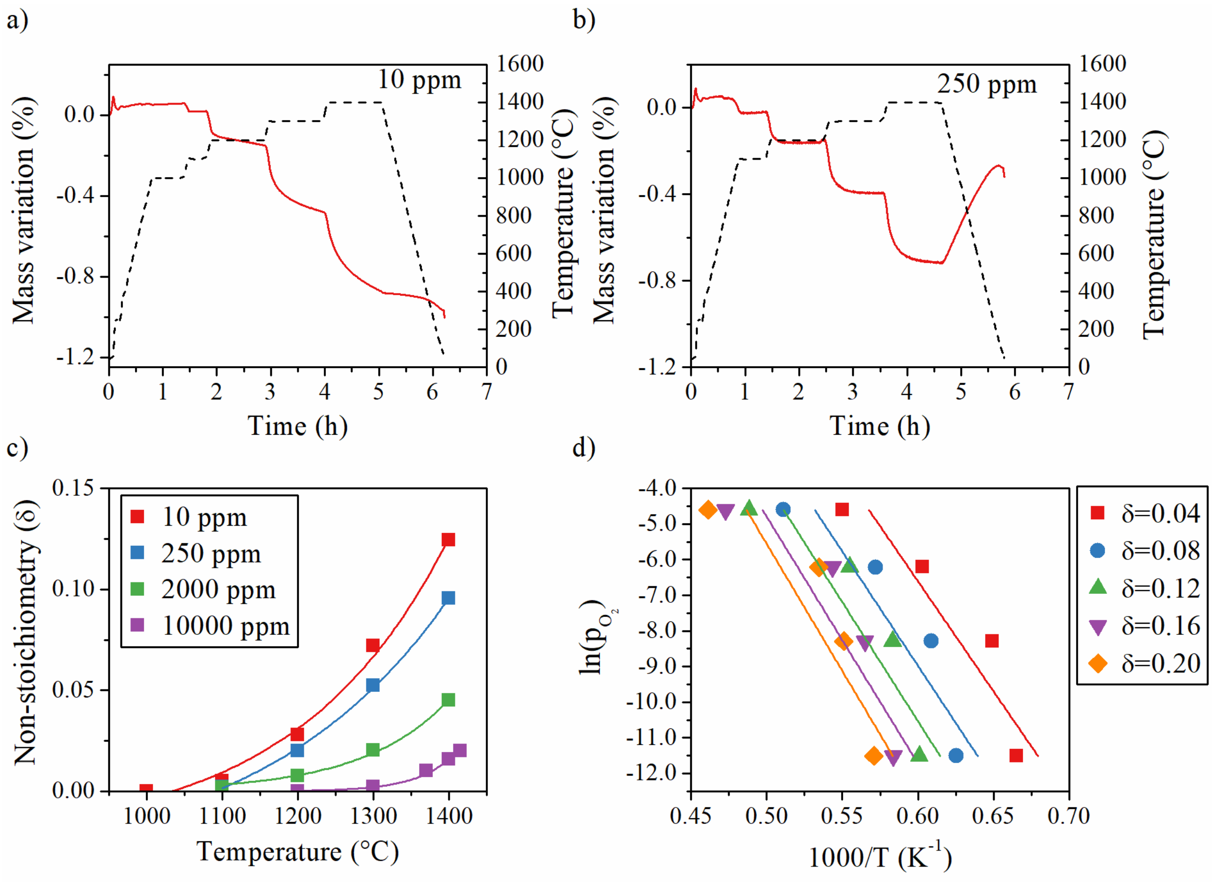

Figure 9: a) TGA of LSMMg under 10 ppm O_2 and b) TGA of LSMMg under 250 ppm O_2 with successive temperature steps (heating rate of 20°C/min, dwell of 60 min), c) non-stoichiometry extent as a function of temperature, and d) logarithm of oxygen partial pressure versus inverse temperature for LSMMg

The thermodynamic properties of both materials were investigated with calculation of their partial molar enthalpies and entropies as a function of oxygen non-stoichiometry (Figure 10). The enthalpy and entropy values for CeO_2 and $La_{0.5}Sr_{0.5}MnO_3$ (LSM) calculated by [18,67] were also plotted for comparison. Both LSM and LSMMg show similar and consistent trends because the materials have close redox activity, which confirms experimental data reliability. CSM features large oxygen non-stoichiometry variation and an increase of entropy and enthalpy values with the increase of non-stoichiometry (in the δ range 0.1-0.32 related to the experimental measurements), as also previously noticed for several other perovskite materials that reproduced a similar trend [68–72]. Figure 11 presents the evolution of the Gibbs free enthalpy (ΔG) as a function of the non-stoichiometry extent for a temperature of 1400°C under 10 ppm O_2. For both CSM and LSMMg-P1, ΔG values constantly increase with the increase of non-stoichiometry. This can be explained by the fact that increasing the non-stoichiometry requires increasing the energy input to the reaction.

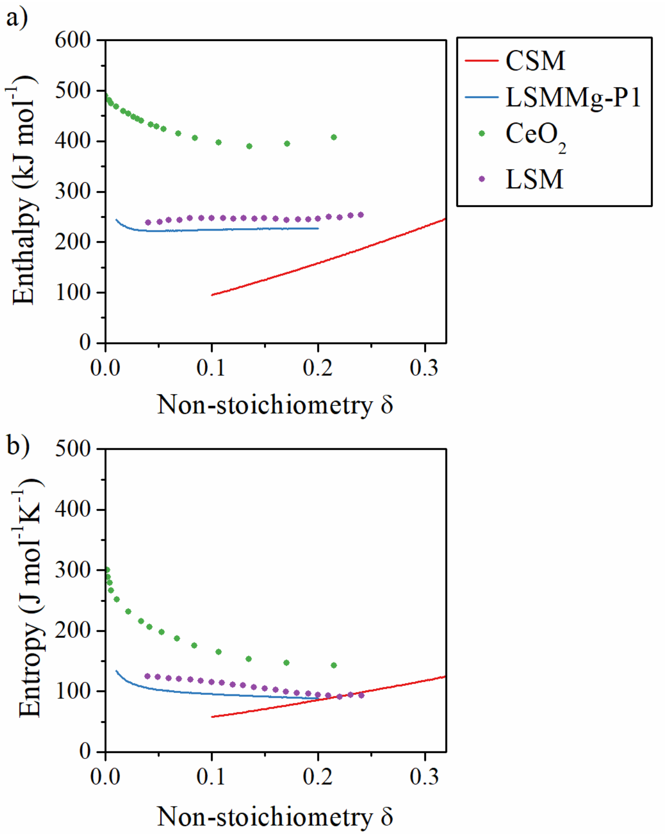

Figure 10: a) Enthalpy and b) entropy of reduction as a function of the oxygen non-stoichiometry for CSM and LSMMg. Data for CeO_2 *and LSM issued from [18,67] were also reported for comparison purpose*

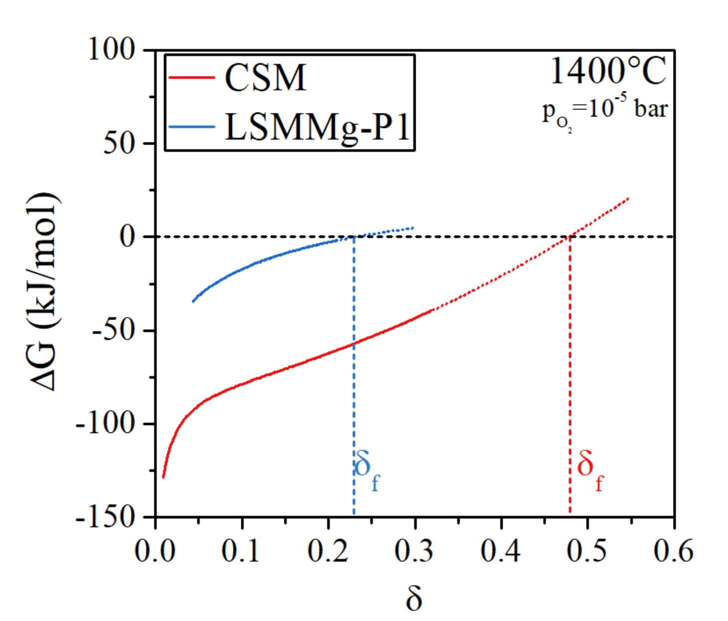

Figure 11: Gibbs free enthalpy at 1400°C under 10 ppm O_2 versus the non-stoichiometry extent for CSM and LSMMg

From the knowledge of the enthalpy and entropy values, it is possible to determine the theoretical maximum non-stoichiometry extent for both the oxidation and reduction steps. In the following, both the reduction extent and re-oxidation yield of CSM and LSMMg in similar conditions than TGA (reduction at 1400°C under 10 ppm O_2 with a re-oxidation step at 1050°C) are predicted thanks to the thermodynamic data extracted from the previous analysis. At the reaction equilibrium, the Gibbs free enthalpy of the reaction is null. To obtain the final non-stoichiometry extent (δ_f), the non-standard Gibbs free enthalpy needs to be determined as a function of non-stoichiometry. Thus, for fixed operating conditions, the reduction extent at equilibrium, which corresponds to a null Gibbs free enthalpy, is the final reduction extent obtained from equation (2).

$$\Delta G_o(\delta_f) = \Delta H_o(\delta_f) - T_{red}\Delta S_o(\delta_f) + \frac{1}{2}RT\ln\left(\frac{p_{O_2}}{P^{\circ}}\right) = 0 \tag{2}$$

The values of the final oxygen non-stoichiometry of CSM and LSMMg after the reduction step thus derive from the vertical dashed lines corresponding to $\Delta G = 0$ in Figure 11.

Concerning the oxidation step, it is also possible to determine the maximum non-stoichiometry reached after the re-oxidation reaction (δ_{ox}). The re-oxidation of the reduced material ($M_xO_{y-\delta_{red}}$)

with CO_2 (reaction 3) is the sum of the material oxidation with O_2 (reaction 4) and the CO_2 dissociation (reaction 5).

$$\frac{1}{\Delta\delta}\mathrm{M_xO}_{\mathrm{y}-\delta_{red}} + \mathrm{CO_2} \rightarrow \frac{1}{\Delta\delta}\mathrm{M_xO}_{\mathrm{y}-\delta_{ox}} + \mathrm{CO} \tag{3}$$

$$\frac{1}{\Delta\delta}\mathrm{M_xO}_{\mathrm{y}-\delta_{red}} + \frac{1}{2}\mathrm{O_2} \rightarrow \frac{1}{\Delta\delta}\mathrm{M_xO}_{\mathrm{y}-\delta_{ox}} \tag{4}$$

$$\mathrm{CO_2} \rightarrow \mathrm{CO} + \frac{1}{2}\mathrm{O_2} \tag{5}$$

Thus, the Gibbs enthalpy of re-oxidation reaction is the sum of Gibbs enthalpy of the two previous reactions, as defined by equation (6),

$$\Delta G^{\circ}_{re-ox} = -\Delta G^{\circ}_{o}(\delta_{ox}) + \Delta G^{\circ}_{\mathrm{CO_2}} \tag{6}$$

Where ΔG°_{re-ox}, ΔG°_{ox} and $\Delta G^{\circ}_{\mathrm{CO_2}}$ are the standard free energy of reactions (3), (4), and (5) respectively. The equilibrium constant of the CO_2 dissociation can be expressed at 1 atm as:

$$K_{diss} = \frac{p_{\mathrm{CO}} * p_{\mathrm{O_2}}^{1/2}}{p_{\mathrm{CO_2}} * P^{\circ 1/2}} \tag{7}$$

Where K_{diss} is the dissociation constant, p_{CO}, $p_{\mathrm{O_2}}$, and $p_{\mathrm{CO_2}}$ the partial pressure of CO, O_2 and CO_2, respectively. The CO yields at equilibrium can be determined by expressing the oxygen partial pressure in terms of the dissociation constant, and values of CO_2 and CO partial pressures, as shown in equation (8).

$$\Delta G_O(\delta_{red} - \Delta\,\delta) = RT_{ox}\ln\left[\frac{K_{diss}p_{\mathrm{CO_2}}}{p_{\mathrm{CO}}}\right] \tag{8}$$

The CO_2 and CO partial pressures can be expressed according to the following equations:

$$p_{\mathrm{CO_2}} = \frac{n_{\mathrm{CO_2},i} - n_{\mathrm{CO}}}{n_g} \tag{9}$$

$$p_{CO} = \frac{n_{\mathrm{CO}}}{n_g} \tag{10}$$

Where $n_{\mathrm{CO}_2,i}$, n_{CO}, n_g are the initial amount of CO_2, the amount of CO and the total amount of gas per mole of reactive material, respectively. Combining the equations (8), (9), and (10) allows to determine the amount of CO produced per mole of material, and corresponding to $\Delta\delta$. It is assumed that the reaction occurs in a closed-system and that spontaneous CO_2 dissociation is not significant at the oxidation temperature. Similar reasoning can be applied for an oxidation step using water as oxidant gas [73–76]. Using the method previously exposed, the theoretical reduction extent and fuel production yield for CSM and LSMMg were computed (Table 1), representing the boundary values predicted by thermodynamics. The operating conditions inputted in the thermodynamic model were the followings: reduction step at 1400°C under 10^{-5} bar of O_2 partial pressure, followed by a re-oxidation at 1050°C. The initial amount of oxidant gas was assumed to be in large excess at $n_{\mathrm{CO}_2,i} = 1000\delta_{red}$ as used in [74]. These operating conditions correspond to those used in TGA. In addition, a less favorable initial CO_2 amount for oxidation corresponding to $n_{\mathrm{CO}_2,i} = 10\delta_{red}$ was also considered for comparison. The theoretical final non-stoichiometry extents after the reduction step were calculated at δ=0.475 and 0.231 for CSM and LSMMg-P1, respectively. Thus, CSM reached a higher reduction extent than LSMMg-P1 at equilibrium (O_2 production: 1469 µmol/g for CSM and 542 µmol/g for LSMMg-P1). This is due to the lower enthalpy for CSM in comparison with LSMMg-P1, which permits to reach higher final non-stoichiometry. Concerning the oxidation step, LSMMg-P1 presents a high re-oxidation yield (72%), whereas it is only 32% for CSM at 1050°C for $n_{\mathrm{CO}_2,i} = 1000\delta_{red}$. Indeed, CSM exhibits a too low enthalpy to allow full re-oxidation. A decrease in the initial amount of excess CO_2 to $10\delta_{red}$ leads to the re-oxidation yield decrease (decrease of $\Delta\delta$ in Table 1). The comparison between the theoretical and experimental values obtained with TGA shows a large disparity. This can be explained by the limited cycling duration used in TGA, impeding reaction completion, whereas the thermodynamic equilibrium study does not consider reaction kinetics. Secondly as the reduction step is not complete, then during the re-oxidation step, the non-stoichiometry variation is lower. This analysis confirmed that the very different redox behavior of CSM (high reducibility and low oxidation capability with CO_2) in comparison with LSMMg can be predicted from thermodynamic properties derived from experimental $\delta(T,p_{O2})$ measurements. Thus, the thermodynamic study is a relevant approach to highlight interesting reactive materials for thermochemical cycles, although it must be completed with experimental data and kinetic study of thermochemical cycles.

Table 1: Theoretical non-stoichiometry extents and O_2 *and CO production yields derived from thermodynamic equilibrium investigations (*T_{red}*=1400°C,* $p_{O2,\,red}=10^{-5}$ *bar,* T_{ox}*=1050°C under* CO_2 *excess)*

	Reduction step		Oxidation step					
Compound	δ_{red}	O_2 produced (µmol/g)	δ_{ox} for $n_{CO_2,i} =$ $1000\delta_{red}$	δ_{ox} for $n_{CO_2,i} =$ $10\delta_{red}$	$\Delta\delta$ for $n_{CO_2,i} =$ $1000\delta_{red}$	$\Delta\delta$ for $n_{CO_2,i} =$ $10\delta_{red}$	CO produced for $n_{CO_2,i} =$ $1000\delta_{red}$ (µmol/g)	CO produced for $n_{CO_2,i} =$ $10\delta_{red}$ (µmol/g)
CSM	0.475	1469	0.321	0.344	0.154	0.041	923	246
LSMMg-P1	0.231	542	0.064	0.075	0.167	0.155	784	727

3.3. Kinetic study

The kinetics of redox reactions was investigated to predict the amount of fuel produced by a reactive material as a function of the cycling time. However, the study of reaction kinetics is complex due to the high number of involved parameters. The kinetic rate of a reaction is defined by equation (11),

$$\frac{\mathrm{d}\alpha}{\mathrm{d}t} = A \exp\left(-\frac{E_a}{RT}\right) f(\alpha) \tag{11}$$

where α is the conversion extent, f a mathematical function representing the reaction mechanism, E_a the activation energy, A the pre-exponential factor and T the temperature.

The main reaction models used in solid-state kinetics are presented in Table S3 [77,78]. The nucleation models describe reactions such as crystallization, crystallographic transition or adsorption. The geometrical contraction models assume that the reaction is controlled by the progression of the reaction interface toward the center of a reactive particle. Diffusion models represent the kinetic mechanism in a reaction that is controlled by the thickness of the product barrier. While in the order-based models, the reaction rate is proportional to the concentration of remaining reactants. In this study, two approaches are proposed to investigate the kinetics of the reduction reaction. The first one is a simple method requiring experimental data with only one heating rate, which provides a first evaluation of the activation energy. The second method requires performing the reduction reaction with at least three different temperature ramps and permits to obtain the activation energy as a function of the conversion extent.

3.3.1. Direct method to determine the activation energy

The first method permits to calculate the apparent activation energy of the reduction reaction by assuming that the reaction mechanism is unchanged during the process. Rewriting the general kinetic equation (11) gives equation (12).

$$\ln\left(\frac{\mathrm{d}\alpha/\mathrm{d}t}{f(\alpha)}\right) = \ln(A) - \frac{E_a}{RT} \tag{12}$$

By plotting $\ln\left(\frac{\mathrm{d}\alpha/\mathrm{d}t}{f(\alpha)}\right)$ as a function of $1/T$, the activation energy is calculated by linear regression. This method requires knowing the reaction model function and thus the contracting sphere model (R3) was used, assuming that the reaction proceeds from the external surface to the core of particles [79]. Indeed the contracting sphere model (R3) offers the best fitting of experimental data (as shown in Figure S13, comparing with A3 and F3 models). The activation energies for all the investigated materials were calculated with this method, using TGA data (heating to 1400°C at 20°C/min in Ar). Figure 12 represents the O_2 production yield of all the investigated reactive materials as a function of the activation energy of the reduction reaction. The hollowed scatters represent data with high residual standard deviation value during the linear regression. Within a given material family, the increase of activation energy was clearly correlated to the decrease of O_2 production yield. Indeed, the activation energy represents the energy barrier that should be overpassed to perform a reaction. Consequently, the activation energy can be used as an indicator to predict the non-stoichiometry reached by a reactive material. However, it does not give any indication on the oxidation step, impeding to predict the amount of fuel produced. The correlation existing between the non-stoichiometry extent and the activation energy is further emphasized in the next section in the case of LSMMg reduction.

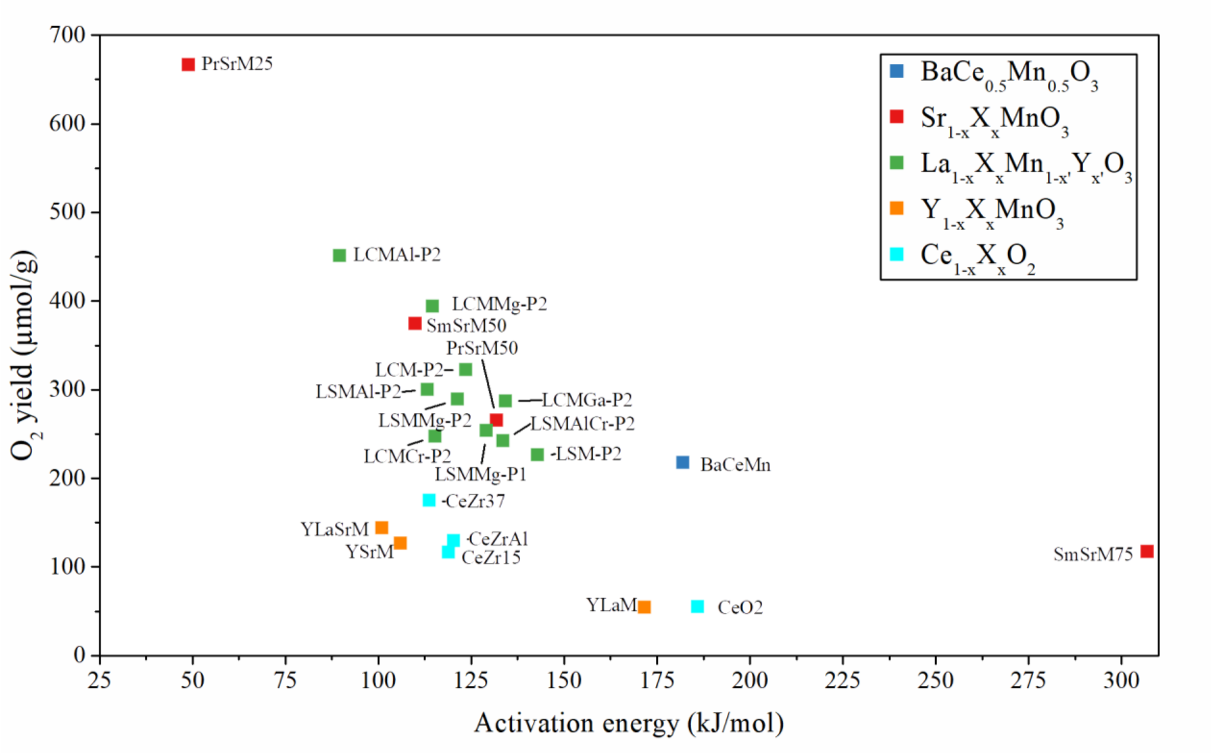

Figure 12: Experimental O_2 yield as a function of activation energy for the series of investigated reactive materials

3.3.2. Iso-conversion method

The activation energy as a function of the conversion extent can be obtained thanks to the iso-conversion method. It assumes that, for a fixed conversion extent, the reaction rate only depends on the temperature, as expressed by equation (13).

$$\left[\frac{\partial \ln\left(\frac{\mathrm{d}\alpha}{\mathrm{d}t}\right)}{\partial T^{-1}}\right]_{\alpha} = -\frac{E_\alpha}{R} \tag{13}$$

Numerous iso-conversional computational methods exist, using the same principle. In this study, the differential iso-conversional method developed by Friedman [80] was used. It is based on equation (14):

$$\ln\left(\frac{\mathrm{d}\alpha}{\mathrm{d}t}\right)_{\alpha,i} = \ln[f(\alpha)A_\alpha] - \frac{E_\alpha}{RT_{\alpha,i}} \tag{14}$$

where i denotes the heating rate, $T_{\alpha,i}$ is the temperature at which α is reached under the heating rate i. Plotting $\ln\left(\frac{d\alpha}{dt}\right)_{\alpha,i}$ as a function of $1/T_{\alpha,i}$ allows obtaining the activation energy for each α value determined from the slope of the plot (Figure 13). The method is model-free, as it does not require any reaction model assumption. Complex reaction mechanisms can even be highlighted by a discontinuity of the activation energy as a function of the conversion extent. Three temperature ramps were performed in TGA, as illustrated in Figure 13a. The rates from TGA measurements were assumed not being affected by mass transfer limitations given the low solid mass involved (gas phase oxygen diffusion is not limiting) and the sweep gas flow rate was kept unchanged during the tests at different heating rates. The conversion extent was defined as the ratio of the non-stoichiometry extent to the final non-stoichiometry extent. The latter was assumed to be the theoretical final non-stoichiometry extent at 1400°C under 10 ppm O_2 (calculated in the thermodynamic study). The non-stoichiometry evolution as a function of temperature for 3°C/min and 5°C/min ramps are very similar (but different) because the temperature ramps are very close. The non-stoichiometry interval in which the activation energy was determined corresponds to the non-stoichiometry values reached at the different temperatures during heating, since the iso-conversional method required using different temperatures for a given α value.

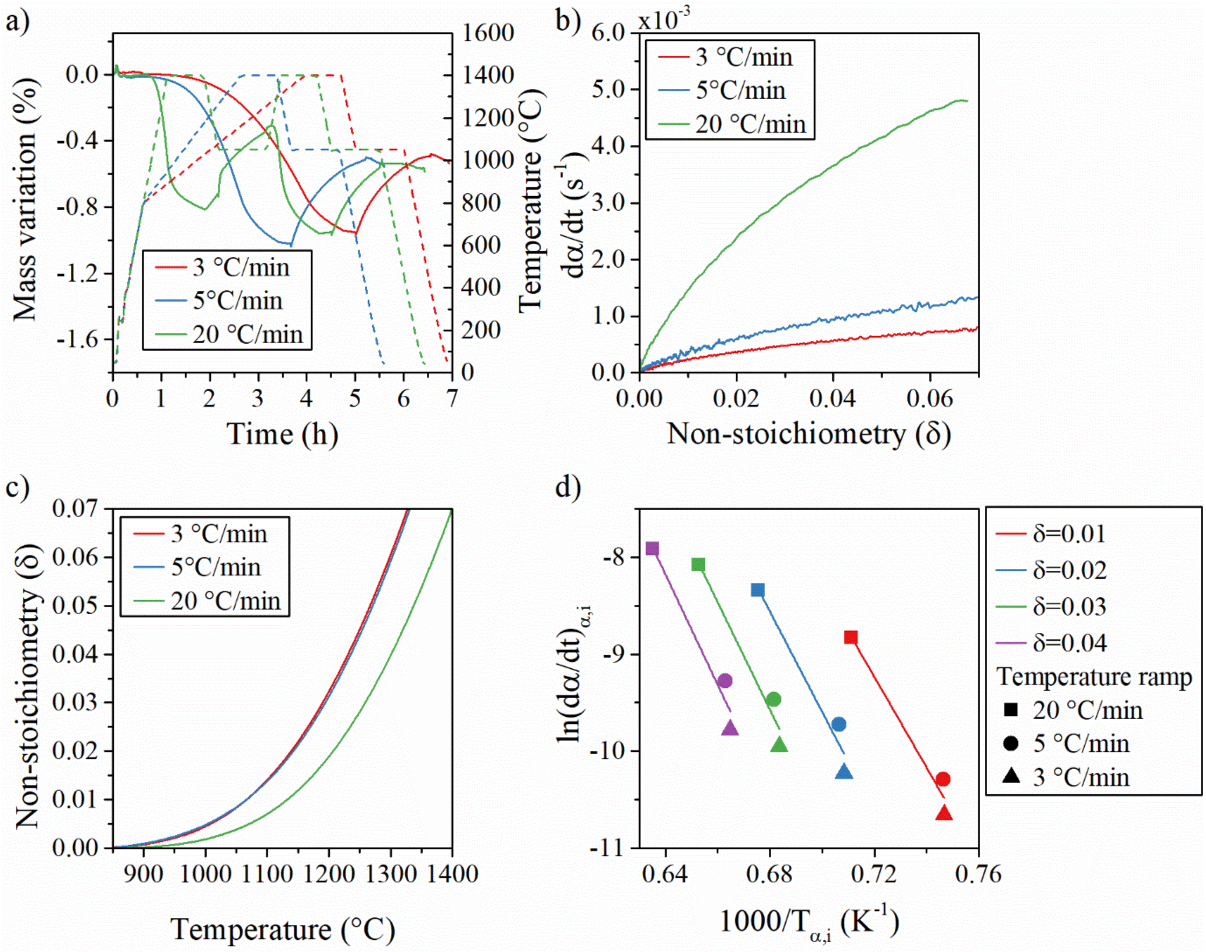

Figure 13: a) Mass variation during TGA of LSMMg for different heating rates under Ar (3°C/min, 5°C/min, and 20°C/min) along with the associated temperature profiles. The mass loss during the first reduction step at the different heating rates was used for kinetic analysis (after reduction, the material was re-oxidized at 1050°C under 50% CO_2 in Ar). b) associated conversion extent as function of non-stoichiometry, c) associated non-stoichiometry extent as a function of temperature, and d) logarithm of the reaction rate as a function of the inverse temperature for different non-stoichiometry extents at constant heating rates

The activation energy for the reduction of LSMMg-P1 was computed with this method (Figure 14). The evolution of the activation energy versus non-stoichiometry extent does not show any discontinuity, revealing a single reaction mechanism during the reduction step. The activation energy is not constant with the evolution of the reduction extent: it increases from ~300 kJ/mol up to ~500 kJ/mol when non-stoichiometry increases. This means that the reduction of LSMMg-P1 becomes more kinetically limited as oxygen extraction proceeds, and the reduction reaction is thus increasingly hindered. This result confirms the relevance of activation energy determination versus non-stoichiometry during the reduction reaction. The iso-conversion method provides relevant information about the kinetic behavior of reactive materials for thermochemical cycles. Regarding the oxidation step, such methods are not applicable because the oxidation step is thermodynamically favored by a temperature decrease in the investigated temperature range, thus implying a thermodynamic control of the reaction.

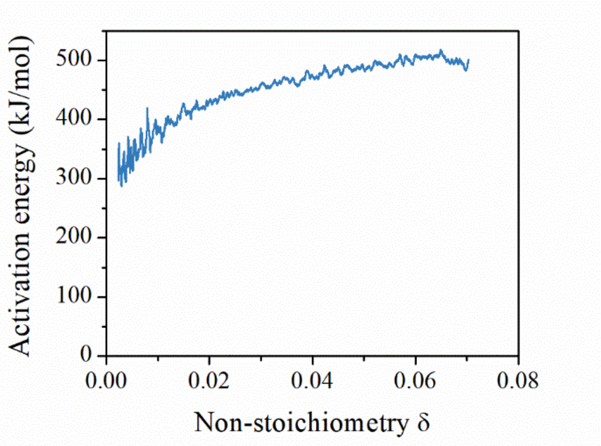

Figure 14: Activation energy of LSMMg reduction as a function of the non-stoichiometry extent

4. Conclusion

A large range of materials compositions was probed in order to identify suitable formulations for thermochemical cycles with potentially high solar-to-fuel conversion efficiency. The materials were experimentally screened to unveil the variations in redox reactivity. In comparison with ceria, considered as the benchmark material, numerous perovskites offer improved thermochemical performance related to both reduction extent and fuel production capacity, such as $(La,A)(B,Mn)O_3$ (with A=Ca and Sr and B=Al, Al/Cr, Cr, Ga and Mg), $(Y,La)SrMnO_3$, $(Pr,Sr)MnO_3$, and $(Sm,Sr)MnO_3$. LSMMg exhibits promising performance, combining high reduction extent, high fuel production yield, and good thermal stability. In addition, $Ca_{0.5}Sr_{0.5}MnO_3$ (CSM) was also investigated due to its high reduction capability and oxygen mobility, potentially attractive for ceramic membrane applications (requiring enhanced oxygen ion transport). Kinetic and/or thermodynamic properties of

LSMMg and CSM were extracted from different experiments to provide further insights on their redox activity.

It has been demonstrated that in $A_{1-x}Sr_xMnO_3$ perovskites, Sm^{3+} and Pr^{3+} in A-site permit to increase the reduction extent in comparison with La^{3+} but the re-oxidation yield is not enhanced as well. The extent of Sr^{2+} substitution impacts on the perovskite reduction extent as it modifies the Mn oxidation state. Among the lanthanum-manganite perovskites, Ca^{2+} dopant in A-site permits to increase the amount of oxygen released in comparison with Sr^{2+} but not the fuel production yield. For LSM, doping with Ga^{3+}, Al^{3+} and Mg^{2+} brings about an improvement of the amount of oxygen and fuel produced. On the contrary, doping with Cr or Al/Cr negatively impacts on LSM thermochemical performance.

For doped-ceria, the increase of Zr^{4+} incorporation enhances the reduction extent. The optimal Zr content appears to be 15% as it increases both the oxygen and fuel production yields. Conversely, co-doping with Al^{3+}/Zr^{4+} does not improve ceria thermochemical cycles.

Regarding kinetics, it has been highlighted that the activation energy of the reduction step is correlated with the reduction extent of the reactive material. Moreover, the activation energy increases with the increase of non-stoichiometry extent during the progression of the reduction reaction. However, reduction kinetics does not allow anticipating the re-oxidation rate/yield, which is also a key factor for materials selection. In addition, the determination of thermodynamic properties permits to predict the theoretical reduction and re-oxidation extent, but experimental values can be lower than those predicted at thermodynamic equilibrium due to kinetic limitations. Thus, it is essential to combine both kinetic and thermodynamic studies, in order to provide the most complete overview of the redox behavior of the selected reactive materials.

Acknowledgments

This work was funded by the French National Agency for Research (ANR, SUNFUEL project, contract N°ANR-16-CE06-0010). The authors thank J. Jouannaux for P2-powders synthesis.

Supplementary material

Supplementary Tables (list of materials formulations, O_2 and CO production yields, usual kinetic models for solid-state reactions), calculation of O_2 and CO yields from TGA, tubular furnace experiments, supplementary Figures (structural characterization of materials, redox activity tests).

References

[1] C.L. Muhich, B.D. Ehrhart, I. Al-Shankiti, B.J. Ward, C.B. Musgrave, A.W. Weimer, A review and perspective of efficient hydrogen generation via solar thermal water splitting, WIREs Energy Environ. 5 (2015) 261–287. https://doi.org/10.1002/wene.174.

[2] S. Abanades, P. Charvin, G. Flamant, P. Neveu, Screening of water-splitting thermochemical cycles potentially attractive for hydrogen production by concentrated solar energy, Energy. 31 (2006) 2805–2822. https://doi.org/10.1016/j.energy.2005.11.002.

[3] G. Centi, S. Perathoner, Opportunities and prospects in the chemical recycling of carbon dioxide to fuels, Catal. Today. 148 (2009) 191–205. https://doi.org/10.1016/j.cattod.2009.07.075.

[4] S. Abanades, Thermogravimetry Analysis of CO_2 and H_2O Reduction from Solar Nanosized Zn Powder for Thermochemical Fuel Production, Ind. Eng. Chem. Res. 51 (2012) 741–750. https://doi.org/10.1021/ie202518k.

[5] S. Abanades, A. Legal, A. Cordier, G. Peraudeau, G. Flamant, A. Julbe, Investigation of reactive cerium-based oxides for H_2 production by thermochemical two-step water-splitting, J. Mater. Sci. 45 (2010) 4163–4173. https://doi.org/10.1007/s10853-010-4506-4.

[6] F. Call, M. Roeb, M. Schmücker, C. Sattler, R. Pitz-Paal, Ceria Doped with Zirconium and Lanthanide Oxides to Enhance Solar Thermochemical Production of Fuels, J. Phys. Chem. C. 119 (2015) 6929–6938. https://doi.org/10.1021/jp508959y.

[7] P. Charvin, S. Abanades, E. Beche, F. Lemont, G. Flamant, Hydrogen production from mixed cerium oxides via three-step water-splitting cycles, Solid State Ionics. 180 (2009) 1003–1010. https://doi.org/10.1016/j.ssi.2009.03.015.

[8] S. Abanades, I. Villafan-Vidales, CO_2 valorisation based on Fe_3O_4/FeO thermochemical redox reactions using concentrated solar energy, Int. J. Energy Res. 37 (2013) 598–608. https://doi.org/10.1002/er.1953.

[9] T. Kodama, Y. Kondoh, R. Yamamoto, H. Andou, N. Satou, Thermochemical hydrogen production by a redox system of ZrO_2-supported Co(II)-ferrite, Sol. Energy. 78 (2005) 623–631. https://doi.org/10.1016/j.solener.2004.04.008.

[10] J.E. Miller, M.D. Allendorf, R.B. Diver, L.R. Evans, N.P. Siegel, J.N. Stuecker, Metal oxide composites and structures for ultra-high temperature solar thermochemical cycles, J. Mater. Sci. 43 (2008) 4714–4728. https://doi.org/10.1007/s10853-007-2354-7.

[11] P.G. Loutzenhiser, M.E. Gálvez, I. Hischier, A. Stamatiou, A. Frei, A. Steinfeld, CO_2 Splitting via Two-Step Solar Thermochemical Cycles with Zn/ZnO and FeO/Fe $_3O_4$ Redox Reactions II: Kinetic Analysis, Energ. Fuel. 23 (2009) 2832–2839. https://doi.org/10.1021/ef801142b.

[12] C. Agrafiotis, A. Zygogianni, C. Pagkoura, M. Kostoglou, A.G. Konstandopoulos, Hydrogen production via solar-aided water splitting thermochemical cycles with nickel ferrite: Experiments and modeling, AlChE J. 59 (2013) 1213–1225. https://doi.org/10.1002/aic.13882.

[13] C. Milone, Y. Kato, E. Mastronardo, Thermal Energy Storage with Chemical Reactions, in: A. Frazzica, L.F. Cabeza (Eds.), Recent Advancements in Materials and Systems for Thermal Energy Storage, Springer International Publishing, Cham, 2019: pp. 15–32. https://doi.org/10.1007/978-3-319-96640-3_3.

[14] B. Bulfin, J. Vieten, C. Agrafiotis, M. Roeb, C. Sattler, Applications and limitations of two step metal oxide thermochemical redox cycles; a review, J. Mater. Chem. A. 5 (2017) 18951–18966. https://doi.org/10.1039/C7TA05025A.

[15] A. Haeussler, S. Abanades, J. Jouannaux, A. Julbe, Non-Stoichiometric Redox Active Perovskite Materials for Solar Thermochemical Fuel Production: A Review, Catalysts. 8 (2018) 611–631. https://doi.org/10.3390/catal8120611.

[16] Abanades, Metal Oxides Applied to Thermochemical Water-Splitting for Hydrogen Production Using Concentrated Solar Energy, ChemEngineering. 3 (2019) 63. https://doi.org/10.3390/chemengineering3030063.

[17] R.J. Carrillo, J.R. Scheffe, Advances and trends in redox materials for solar thermochemical fuel production, Sol. Energy. 156 (2017) 3–20. https://doi.org/10.1016/j.solener.2017.05.032.

[18] C.-K. Yang, Y. Yamazaki, A. Aydin, S.M. Haile, Thermodynamic and kinetic assessments of strontium-doped lanthanum manganite perovskites for two-step thermochemical water splitting, J. Mater. Chem. A. 2 (2014) 13612–13623. https://doi.org/10.1039/C4TA02694B.

[19] M.E. Gálvez, R. Jacot, J. Scheffe, T. Cooper, G. Patzke, A. Steinfeld, Physico-chemical changes in Ca, Sr and Al-doped La–Mn–O perovskites upon thermochemical splitting of CO_2 via redox cycling, Phys. Chem. Chem. Phys. 17 (2015) 6629–6634. https://doi.org/10.1039/C4CP05898D.

[20] A. Demont, S. Abanades, Solar thermochemical conversion of CO_2 into fuel via two-step redox cycling of non-stoichiometric Mn-containing perovskite oxides, J. Mater. Chem. A. 3 (2015) 3536–3546. https://doi.org/10.1039/C4TA06655C.

[21] T. Cooper, J.R. Scheffe, M.E. Galvez, R. Jacot, G. Patzke, A. Steinfeld, Lanthanum Manganite Perovskites with Ca/Sr A-site and Al B-site Doping as Effective Oxygen Exchange Materials for Solar Thermochemical Fuel Production, Energy Technol. 3 (2015) 1130–1142. https://doi.org/10.1002/ente.201500226.

[22] L. Wang, M. Al-Mamun, Y.L. Zhong, L. Jiang, P. Liu, Y. Wang, H.G. Yang, H. Zhao, Ca^{2+} and Ga^{3+} doped $LaMnO_3$ perovskite as a highly efficient and stable catalyst for two-step thermochemical water splitting, Sustainable Energy Fuels. 1 (2017) 1013–1017. https://doi.org/10.1039/C6SE00097E.

[23] M.M. Nair, S. Abanades, Experimental screening of perovskite oxides as efficient redox materials for solar thermochemical CO_2 conversion, Sustainable Energy Fuels. 2 (2018) 843–854. https://doi.org/10.1039/C7SE00516D.

[24] J. Jouannaux, A. Haeussler, M. Drobek, A. Ayral, S. Abanades, A. Julbe, Lanthanum manganite perovskite ceramic powders for CO_2 splitting: Influence of Pechini synthesis parameters on sinterability and reactivity, Ceram. Int. 45 (2019) 15636–15648. https://doi.org/10.1016/j.ceramint.2019.05.075.

[25] A.H. McDaniel, E.C. Miller, D. Arifin, A. Ambrosini, E.N. Coker, R. O'Hayre, W.C. Chueh, J. Tong, Sr- and Mn-doped $LaAlO_{3-\delta}$ for solar thermochemical H_2 and CO production, Energ. Environ. Sci. 6 (2013) 2424–2428. https://doi.org/10.1039/c3ee41372a.

[26] S. Dey, B.S. Naidu, C.N.R. Rao, Beneficial effects of substituting trivalent ions in the B-site of $La_{0.5}Sr_{0.5}Mn_{1-x}A_xO_3$ (A = Al, Ga, Sc) on the thermochemical generation of CO and H_2 from CO_2 and H_2O, Dalton Trans. 45 (2016) 2430–2435. https://doi.org/10.1039/C5DT04822B.

[27] M.M. Nair, S. Abanades, Insights into the Redox Performance of Non-stoichiometric Lanthanum Manganite Perovskites for Solar Thermochemical CO_2 Splitting, ChemistrySelect. 1 (2016) 4449–4457. https://doi.org/10.1002/slct.201601171.

[28] A. Haeussler, S. Abanades, J. Jouannaux, A. Julbe, Demonstration of a ceria membrane solar reactor promoted by dual perovskite coatings for continuous and isothermal redox splitting of CO2 and H2O, Journal of Membrane Science. 634 (2021) 119387. https://doi.org/10.1016/j.memsci.2021.119387.

[29] A. Haeussler, S. Abanades, A. Julbe, J. Jouannaux, B. Cartoixa, Two-step CO2 and H2O splitting using perovskite-coated ceria foam for enhanced green fuel production in a porous volumetric solar reactor, Journal of CO2 Utilization. 41 (2020) 101257. https://doi.org/10.1016/j.jcou.2020.101257.

[30] T.O.L. Sunde, T. Grande, M.-A. Einarsrud, Modified Pechini synthesis of oxide powders and thin films, in: Handbook of Sol-Gel Science and Technology, Springer, 2016.

[31] M.P. Pechini, Method of preparing lead and alkaline earth titanates and niobates and coating method using the same to form a capacitor, US3330697A, 1967. https://patents.google.com/patent/US3330697A/en (accessed April 21, 2020).

[32] G.B.J. de Boer, C. de Weerd, D. Thoenes, H.W.J. Goossens, Laser Diffraction Spectrometry: Fraunhofer Diffraction Versus Mie Scattering, Particle & Particle Systems Characterization. 4 (1987) 14–19. https://doi.org/10.1002/ppsc.19870040104.

[33] S.P. Jiang, Development of lanthanum strontium manganite perovskite cathode materials of solid oxide fuel cells: a review, J. Mater. Sci. 43 (2008) 6799–6833. https://doi.org/10.1007/s10853-008-2966-6.

[34] Y. Xue, H. Miao, S. Sun, Q. Wang, S. Li, Z. Liu, $(La_{1-x}Sr_x)_{0.98}MnO_3$ perovskite with A-site deficiencies toward oxygen reduction reaction in aluminum-air batteries, J. Power Sources. 342 (2017) 192–201. https://doi.org/10.1016/j.jpowsour.2016.12.065.

[35] H.-C. Cho, S. Kuramoto, S. Takase, J.-H. Song, Y. Shimizu, Sensing Properties of Impedancemetric Solid-Electrolyte NO_x Sensor Using Perovskite-Type Lanthanum Manganite-Based Receptor, Sens. Mater. 24 (2012) 31. https://doi.org/10.18494/SAM.2012.763.

[36] M.R. Mullen, J.V. Spirig, J. Hoy, J.L. Routbort, D. Singh, P.K. Dutta, Development of nanosized lanthanum strontium aluminum manganite as electrodes for potentiometric oxygen sensor, Sensors and Actuators B: Chemical. 203 (2014) 670–676. https://doi.org/10.1016/j.snb.2014.07.027.

[37] S. Ponce, M.A. Peña, J.L.G. Fierro, Surface properties and catalytic performance in methane combustion of Sr-substituted lanthanum manganites, Appl. Catal. B Environ. 24 (2000) 193–205. https://doi.org/10.1016/S0926-3373(99)00111-3.

[38] G.J. la O', Y. Shao-Horn, Thickness Dependence of Oxygen Reduction Reaction Kinetics on Strontium-Substituted Lanthanum Manganese Perovskite Thin-Film Microelectrodes, Electrochem. Solid-State Lett. 12 (2009) B82. https://doi.org/10.1149/1.3095681.

[39] J.R. Scheffe, D. Weibel, A. Steinfeld, Lanthanum–Strontium–Manganese perovskites as redox materials for solar thermochemical splitting of H_2O and CO_2, Energ. Fuel. 27 (2013) 4250–4257. https://doi.org/10.1021/ef301923h.

[40] A.L.A. da Silva, L. da Conceição, A.M. Rocco, M.M.V.M. Souza, Synthesis of Sr-doped $LaMnO_3$ and $LaCrO_3$ powders by combustion method: structural characterization and thermodynamic evaluation, Cerâmica. 58 (2012) 521–528. https://doi.org/10.1590/S0366-69132012000400018.

[41] J.E. Miller, A. Ambrosini, E.N. Coker, M.D. Allendorf, A.H. McDaniel, Advancing Oxide Materials for Thermochemical Production of Solar Fuels, Energy Procedia. 49 (2014) 2019–2026. https://doi.org/10.1016/j.egypro.2014.03.214.

[42] C. Agrafiotis, M. Roeb, C. Sattler, A review on solar thermal syngas production via redox pair-based water/carbon dioxide splitting thermochemical cycles, Renew. Sustain. Energ. Rev. 42 (2015) 254–285. https://doi.org/10.1016/j.rser.2014.09.039.

[43] A. Demont, S. Abanades, E. Beche, Investigation of Perovskite Structures as Oxygen-Exchange Redox Materials for Hydrogen Production from Thermochemical Two-Step Water-Splitting Cycles, J. Phys. Chem. C. 118 (2014) 12682–12692. https://doi.org/10.1021/jp5034849.

[44] A.H. Bork, E. Povoden-Karadeniz, J.L.M. Rupp, Modeling Thermochemical Solar-to-Fuel Conversion: CALPHAD for Thermodynamic Assessment Studies of Perovskites, Exemplified for $(La,Sr)MnO_3$, Adv. Energy Mater. 7 (2017) 1601086. https://doi.org/10.1002/aenm.201601086.

[45] J.H. Kuo, H.U. Anderson, D.M. Sparlin, Oxidation-reduction behavior of undoped and Sr-doped $LaMnO_3$ nonstoichiometry and defect structure, J. Solid State Chem. 83 (1989) 52–60. https://doi.org/10.1016/0022-4596(89)90053-4.

[46] J. Mizusaki, Oxygen nonstoichiometry and defect equilibrium in the perovskite-type oxides $La_{1-x}Sr_xMnO_{3+d}$, Solid State Ionics. 129 (2000) 163–177. https://doi.org/10.1016/S0167-2738(99)00323-9.

[47] S. Dey, C.N.R. Rao, Splitting of CO_2 by Manganite Perovskites to Generate CO by Solar Isothermal Redox Cycling, ACS Energy Lett. 1 (2016) 237–243. https://doi.org/10.1021/acsenergylett.6b00122.

[48] A. Haeussler, S. Abanades, J. Jouannaux, M. Drobek, A. Ayral, A. Julbe, Recent progress on ceria doping and shaping strategies for solar thermochemical water and CO_2 splitting cycles, AIMS Materials Science. 6 (2019) 657–684. https://doi.org/10.3934/matersci.2019.5.657.

[49] O. Toulemonde, N. N'Guyen, F. Studer, A. Traverse, Spin State Transition in $LaCoO_3$ with Temperature or Strontium Doping as Seen by XAS, J. Solid State Chem. 158 (2001) 208–217. https://doi.org/10.1006/jssc.2001.9094.

[50] O. Haas, R.P.W.J. Struis, J.M. McBreen, Synchrotron X-ray absorption of $LaCoO_3$ perovskite, J. Solid State Chem. 177 (2004) 1000–1010. https://doi.org/10.1016/j.jssc.2003.10.004.

[51] C. Abughayada, Air separation and oxygen storage properties of hexagonal rare-earth manganites., Doctoral dissertation, Northern Illinois University, 2015. https://commons.lib.niu.edu/handle/10843/18551.

[52] Shannon Radii, (n.d.). http://abulafia.mt.ic.ac.uk/shannon/ptable.php (accessed January 4, 2018).

[53] D. R. Barcellos, M.D. Sanders, J. Tong, A.H. McDaniel, R.P. O'Hayre, $BaCe_{0.25}Mn_{0.75}O_{3-\delta}$ —a promising perovskite-type oxide for solar thermochemical hydrogen production, Energ. Environ. Sci. 11 (2018) 3256–3265. https://doi.org/10.1039/C8EE01989D.

[54] P. Furler, J.R. Scheffe, A. Steinfeld, Syngas production by simultaneous splitting of H_2O and CO_2 via ceria redox reactions in a high-temperature solar reactor, Energ. Environ. Sci. 5 (2012) 6098–6103. https://doi.org/10.1039/C1EE02620H.

[55] B. Bulfin, A.J. Lowe, K.A. Keogh, B.E. Murphy, O. Lübben, S.A. Krasnikov, I.V. Shvets, Analytical Model of CeO_2 Oxidation and Reduction, J. Phys. Chem. C. 117 (2013) 24129–24137. https://doi.org/10.1021/jp406578z.

[56] W.C. Chueh, C. Falter, M. Abbott, D. Scipio, P. Furler, S.M. Haile, A. Steinfeld, High-Flux Solar-Driven Thermochemical Dissociation of CO_2 and H_2O Using Nonstoichiometric Ceria, Science. 330 (2010) 1797–1801. https://doi.org/10.1126/science.1197834.

[57] J.R. Scheffe, A. Steinfeld, Oxygen exchange materials for solar thermochemical splitting of H_2O and CO_2: a review, Mater. Today. 17 (2014) 341–348. https://doi.org/10.1016/j.mattod.2014.04.025.

[58] H. Kong, X. Kong, H. Wang, J. Wang, A strategy for optimizing efficiencies of solar thermochemical fuel production based on nonstoichiometric oxides, Int. J. Hydrogen Energy. (2019). https://doi.org/10.1016/j.ijhydene.2019.05.197.

[59] G. Takalkar, R.R. Bhosale, S. Rashid, F. AlMomani, R.A. Shakoor, A. Al Ashraf, Application of Li-, Mg-, Ba-, Sr-, Ca-, and Sn-doped ceria for solar-driven thermochemical conversion of carbon dioxide, J. Mater. Sci. (2020). https://doi.org/10.1007/s10853-020-04875-1.

[60] A. Le Gal, S. Abanades, Catalytic investigation of ceria-zirconia solid solutions for solar hydrogen production, Int. J. Hydrogen Energy. 36 (2011) 4739–4748. https://doi.org/10.1016/j.ijhydene.2011.01.078.

[61] G. Vlaic, P. Fornasiero, S. Geremia, J. Kašpar, M. Graziani, Relationship between the Zirconia-Promoted Reduction in the Rh-Loaded $Ce_{0.5}Zr_{0.5}O_2$ Mixed Oxide and the Zr–O Local Structure, J. Catal. 168 (1997) 386–392. https://doi.org/10.1006/jcat.1997.1644.

[62] A. Le Gal, S. Abanades, G. Flamant, CO_2 and H_2O Splitting for Thermochemical Production of Solar Fuels Using Nonstoichiometric Ceria and Ceria/Zirconia Solid Solutions, Energ. Fuel. 25 (2011) 4836–4845. https://doi.org/10.1021/ef200972r.

[63] E.I. Goldyreva, I.A. Leonidov, M.V. Patrakeev, A.V. Chukin, I.I. Leonidov, V.L. Kozhevnikov, Oxygen nonstoichiometry and defect equilibrium in electron doped $Ca_{0.6-y}Sr_{0.4}La_yMnO_{3-\delta}$, Journal of Alloys and Compounds. 638 (2015) 44–49. https://doi.org/10.1016/j.jallcom.2015.03.048.

[64] K.J. Albrecht, G.S. Jackson, R.J. Braun, Thermodynamically consistent modeling of redox-stable perovskite oxides for thermochemical energy conversion and storage, Appl. Energy. 165 (2016) 285–296. https://doi.org/10.1016/j.apenergy.2015.11.098.

[65] Y. Hao, C.-K. Yang, S.M. Haile, Ceria–Zirconia Solid Solutions ($Ce_{1-x}Zr_xO_{2-\delta}$, $x \leq 0.2$) for Solar Thermochemical Water Splitting: A Thermodynamic Study, Chem. Mater. 26 (2014) 6073–6082. https://doi.org/10.1021/cm503131p.

[66] J. Vieten, B. Bulfin, P. Huck, M. Horton, D. Guban, L. Zhu, Y. Lu, K.A. Persson, M. Roeb, C. Sattler, Materials design of perovskite solid solutions for thermochemical applications, Energy Environ. Sci. 12 (2019) 1369–1384. https://doi.org/10.1039/C9EE00085B.

[67] R.J. Panlener, R.N. Blumenthal, J.E. Garnier, A thermodynamic study of nonstoichiometric cerium dioxide, J. Phys. Chem. Solids. 36 (1975) 1213–1222. https://doi.org/10.1016/0022-3697(75)90192-4.

[68] X. Qian, J. He, E. Mastronardo, B. Baldassarri, C. Wolverton, S.M. Haile, Favorable Redox Thermodynamics of $SrTi_{0.5}Mn_{0.5}O_{3-\delta}$ in Solar Thermochemical Water Splitting, Chem. Mater. 32 (2020) 9335–9346. https://doi.org/10.1021/acs.chemmater.0c03278.

[69] E. Mastronardo, X. Qian, J.M. Coronado, S.M. Haile, Impact of La doping on the thermochemical heat storage properties of $CaMnO_{3-\delta}$, Journal of Energy Storage. 40 (2021) 102793. https://doi.org/10.1016/j.est.2021.102793.

[70] L. Imponenti, K.J. Albrecht, J.W. Wands, M.D. Sanders, G.S. Jackson, Thermochemical energy storage in strontium-doped calcium manganites for concentrating solar power applications, Solar Energy. 151 (2017) 1–13. https://doi.org/10.1016/j.solener.2017.05.010.

[71] S.M. Babiniec, E.N. Coker, J.E. Miller, A. Ambrosini, Doped calcium manganites for advanced high-temperature thermochemical energy storage, Int. J. Energy Res. 40 (2016) 280–284. https://doi.org/10.1002/er.3467.

[72] J. Vieten, B. Bulfin, M. Senholdt, M. Roeb, C. Sattler, M. Schmücker, Redox thermodynamics and phase composition in the system $SrFeO_{3-\delta}$ — $SrMnO_{3-\delta}$, Solid State Ionics. 308 (2017) 149–155. https://doi.org/10.1016/j.ssi.2017.06.014.

[73] J.R. Scheffe, A. Steinfeld, Thermodynamic Analysis of Cerium-Based Oxides for Solar Thermochemical Fuel Production, Energ. Fuel. 26 (2012) 1928–1936. https://doi.org/10.1021/ef201875v.

[74] M. Takacs, M. Hoes, M. Caduff, T. Cooper, J.R. Scheffe, A. Steinfeld, Oxygen nonstoichiometry, defect equilibria, and thermodynamic characterization of $LaMnO_3$ perovskites with Ca/Sr A-site and Al B-site doping, Acta Mater. 103 (2016) 700–710. https://doi.org/10.1016/j.actamat.2015.10.026.

[75] M. Takacs, J.R. Scheffe, A. Steinfeld, Oxygen nonstoichiometry and thermodynamic characterization of Zr doped ceria in the 1573–1773 K temperature range, Phys. Chem. Chem. Phys. 17 (2015) 7813–7822. https://doi.org/10.1039/C4CP04916K.

[76] W.C. Chueh, S.M. Haile, A thermochemical study of ceria: exploiting an old material for new modes of energy conversion and CO_2 mitigation, Phil. Trans. R. Soc. A. 368 (2010) 3269–3294. https://doi.org/10.1098/rsta.2010.0114.

[77] S. Vyazovkin, A.K. Burnham, J.M. Criado, L.A. Pérez-Maqueda, C. Popescu, N. Sbirrazzuoli, ICTAC Kinetics Committee recommendations for performing kinetic computations on thermal analysis data, Thermochimica Acta. 520 (2011) 1–19. https://doi.org/10.1016/j.tca.2011.03.034.

[78] A. Khawam, D.R. Flanagan, Solid-State Kinetic Models: Basics and Mathematical Fundamentals, J. Phys. Chem. B. 110 (2006) 17315–17328. https://doi.org/10.1021/jp062746a.

[79] O. Levenspiel, Chemical reaction engineering, 3. ed, Wiley, Hoboken, NJ, 1999.

[80] H.L. Friedman, Kinetics of thermal degradation of char-forming plastics from thermogravimetry. Application to a phenolic plastic, J. Polym. Sci., Part C: Polym. Symp. 6 (1964) 183–195. https://doi.org/10.1002/polc.5070060121.